

DATA-DRIVEN REDUCED MODEL CONSTRUCTION WITH TIME-DOMAIN LOEWNER MODELS

BENJAMIN PEHERSTORFER*, SERKAN GUGERCIN†, AND KAREN WILLCOX‡

Abstract. This work presents a data-driven nonintrusive model reduction approach for large-scale time-dependent systems with linear state dependence. Traditionally, model reduction is performed in an intrusive projection-based framework, where the operators of the full model are required either explicitly in an assembled form or implicitly through a routine that returns the action of the operators on a vector. Our nonintrusive approach constructs reduced models directly from trajectories of the inputs and outputs of the full model, without requiring the full-model operators. These trajectories are generated by running a simulation of the full model; our method then infers frequency-response data from these simulated time-domain trajectories and uses the data-driven Loewner framework to derive a reduced model. Only a single time-domain simulation is required to derive a reduced model with the new data-driven nonintrusive approach. We demonstrate our model reduction method on several benchmark examples and a finite element model of a cantilever beam; our approach recovers the classical Loewner reduced models and, for these problems, yields high-quality reduced models despite treating the full model as a black box.

Key words. data-driven model reduction; nonintrusive model reduction; projection-based reduced models; Loewner framework; black-box models; dynamical systems; partial differential equations

AMS subject classifications. 65M22, 65N22

1. Introduction. Projection-based model reduction derives low-cost reduced models with low-dimensional reduced states that approximate the high-dimensional solutions of a large-scale system of equations [2, 10, 47]. Approximating full-model solutions with reduced solutions can reduce the runtime by orders of magnitude; however, the applicability and scope of model reduction is often limited because of the intrusive nature of reduction algorithms. Deriving a reduced model with, e.g., proper orthogonal decomposition [11, 49], balanced truncation [35, 36], the reduced basis method [15, 19, 21, 47], and projection-based interpolatory model reduction [2, 3], is intrusive in the sense that the operators of the full model are required either in an assembled form or through a routine that provides the action of the operators on a given vector. In many situations, however, the full model is given as a black box that computes solutions of the full model without providing the full-model operators. We introduce here a data-driven nonintrusive model reduction approach that constructs a reduced model from the solutions of the full model alone, without requiring the full-model operators.

We consider here time-dependent full models with linear time-invariant (LTI) operators. In our setting, the full models map an input onto an output (quantity of interest) that is obtained via a linear map from the state. Many time-dependent partial differential equations (PDEs) lead to such LTI systems after discretization in the spatial domain. Examples include the heat equation with time-invariant coefficients, equations in dynamic elastic beam and plate theory, and time-dependent convection-diffusion equations with time-invariant coefficients. LTI systems can be represented either in the time domain or in the frequency domain, see, e.g., [2, 10]. The duality

*Department of Mechanical Engineering, University of Wisconsin-Madison, Madison, WI 53706

†Department of Mathematics, Virginia Polytechnic Institute and State University, 460 McBryde, Virginia Tech, Blacksburg, VA 24061-0123

‡Department of Aeronautics & Astronautics, MIT, Cambridge, MA 02139

of the time-domain and the frequency-domain representation allows one to transform a time-domain representation into a frequency-domain representation and vice versa. The map between time-domain representation and frequency-domain representation is given by the Laplace- (or Z-) transform. Reduction techniques building on proper orthogonal decomposition and the reduced basis method are typically formulated in the time domain. In contrast, interpolatory model reduction techniques are typically formulated in the frequency domain, where these techniques interpolate the transfer function of the LTI system. Here we propose to view these frequency-domain reduction techniques through a time-domain lens by exploiting the duality between frequency and time domain. In doing so, we retain the often attractive properties and the analysis of the frequency-domain techniques, but we derive algorithms that apply directly in the time domain. In particular, we build on the Loewner framework, which derives reduced models in the frequency domain from frequency-response data alone, i.e., from evaluations of the transfer function [5, 7, 29, 33]. The Loewner approach therefore provides a nonintrusive way of building a reduced model in the frequency domain. Building on the Laplace- (or Z-) transform to map between frequency and time domain, we derive a nonintrusive data-driven model reduction technique that is based on the Loewner framework and that applies directly to time-domain formulations of, e.g., linear PDEs. Our time-domain Loewner approach is a data-driven nonintrusive model reduction technique that derives a reduced model from the time-domain outputs obtained via time stepping the full model and therefore is applicable even if the full model is given as a black box. Only a single time-domain simulation is required to derive a time-domain Loewner reduced model.

Our approach shares similarities with finite impulse response system identification [1, 30, 34, 45], where the impulse responses of an LTI system are extracted from an input/output trajectory. In [27], the impulse response values are recovered and then used to derive a Loewner reduced model. The number of impulse response coefficients grows with the number of time steps. In contrast, our time-domain Loewner framework directly infers the typically small number of transfer function values, rather than approximating the potentially large number of impulse response coefficients. In [23], an approach to approximate the input/output map of an LTI system from time-domain simulations is introduced. In the first step, finite-dimensional approximate bases are chosen for both the input and the output spaces of the underlying LTI system. In the second step, the LTI system is simulated for each basis vector of the input space and the outputs are projected onto the output basis. This process gives a map, in the form of a finite-dimensional matrix, from the input basis to the output basis, which is then used to approximate the action of the LTI system on other inputs. The construction of the map requires simulating the LTI system for every basis vector of the input space, whereas our approach requires only a single solve of the full model. The approach of [23] is applied to the linearized Navier-Stokes equations in [22]. In [25], exponentials are fitted to input/output trajectories of LTI systems. A nonlinear least-squares problem is solved to obtain the coefficients and the frequency parameters of the exponential fitting. Our approach leads to a linear least-squares problem and therefore avoids the potentially expensive computations required to solve the nonlinear optimization problems as in [25].

Other system identification approaches, such as the eigensystem realization algorithm (ERA), are restricted to situations where impulse responses of the full model are available [28, 44, 46, 51]. Our time-domain Loewner approach constructs a reduced model from output trajectories that are derived from any input; not necessarily im-

pulse responses. If state trajectories are available, then dynamic mode decomposition (DMD) provides a way to find a linear operator that best-fits given state trajectories in the L_2 norm [32, 42, 43, 50]. The work [40] best-fits operators in the L_2 norm similarly to DMD but is applicable also in case of low-order polynomial nonlinear terms. In [12, 42], sparsity-promoting regression techniques are used to assemble a reduced model from a library of model components. In contrast to these techniques that construct reduced models from state trajectories [12, 32, 40, 42, 43, 50], our time-domain Loewner approach is applicable in situations where state trajectories are unavailable.

A different use of data in the model reduction context is the learning of correction terms to account for dynamics of the full model that are missed by reduced models. In [39, 48], corrections to reduced models are inferred with Bayesian inference for several different parameter configurations. The inferred corrections with the corresponding parameter configurations are used as a training set to learn a map from the parameters of the model to the corrections with supervised machine learning techniques. The inference and learning approach presented in [39, 48] is demonstrated on applications in the context of model reduction for turbulent flow models. The work [31, 52] presents a data assimilation framework for correcting the model bias of reduced models with data. Only corrections to available reduced models are learned, whereas our goal is learning a reduced model in a nonintrusive way from data.

Section 2 introduces the class of linear systems considered and discusses the problem setup. Section 3 develops our time-domain Loewner approach and gives a computational procedure to construct a time-domain Loewner reduced model in Algorithm 1. The numerical results in Section 4 demonstrate our time-domain Loewner approach on benchmark problems and a finite element model of a cantilever beam. Section 5 gives concluding remarks.

2. Projection-based model reduction and classical Loewner. Section 2.1 briefly introduces LTI systems, and, in particular, high-dimensional LTI systems that arise from the discretization of time-dependent linear PDEs. Section 2.2 discusses the time-domain and the frequency-domain representation of LTI systems and Section 2.3 introduces projection-based model reduction with the classical Loewner framework. The problem formulation is given in Section 2.4.

2.1. Discretization of time-dependent linear PDEs and LTI systems.

Our starting point is a time-continuous system of ordinary differential equations (ODEs)

$$(2.1) \quad \begin{aligned} \dot{\mathbf{x}}(t) &= \mathbf{a}(\mathbf{x}(t)) + \mathbf{b}(u(t)), \\ y(t) &= \mathbf{c}(\mathbf{x}(t)), \end{aligned}$$

where $N \in \mathbb{N}$ is the number of ODEs, $t \in [0, \infty)$ is time, $\mathbf{x} : [0, \infty) \rightarrow \mathbb{C}^N$ is the state, $\dot{\mathbf{x}}(t)$ is the derivative of \mathbf{x} in time, $\mathbf{a} : \mathbb{C}^N \rightarrow \mathbb{C}^N$ is the linear operator, and $\mathbf{b} : \mathbb{C} \rightarrow \mathbb{C}^N$ is the linear input operator. The input is $u : [0, \infty) \rightarrow \mathbb{C}$. The input is bounded in the sense that a constant $\alpha \in \mathbb{R}$ exists that bounds the absolute value of the input $|u(t)| < \alpha$ for $t \in [0, \infty)$. The output is $y : [0, \infty) \rightarrow \mathbb{C}$ with the linear output operator $\mathbf{c} : \mathbb{C}^N \rightarrow \mathbb{C}$. In this paper, we focus on single-input/single-output systems with zero initial condition $\mathbf{x}(0) = \mathbf{0} \in \mathbb{R}^N$. An extension to multiple-input/multiple-output systems with non-zero initial conditions will be discussed in Section 3.7.

In cases where system (2.1) arises from the spatial discretization of a time-dependent linear PDE, \mathbf{a} arises from the discretization of the PDE operators, and the input u imposes, e.g., the boundary conditions of the corresponding boundary

value problem and control inputs. The output y represents the quantity of interest, which is obtained with the linear functional \mathbf{c} from the state.

Consider now a time step size $0 < \delta t \in \mathbb{R}$ and the time steps $0 = t_0 < t_1 < \dots < t_k < \dots$ with $t_k = k\delta t$ for $k \in \mathbb{N}$. Discretizing system (2.1) in time leads to a time-discrete linear time-invariant (LTI) system of order N

$$(2.2) \quad \Sigma : \begin{cases} \mathbf{E}\mathbf{x}_{k+1} = \mathbf{A}\mathbf{x}_k + \mathbf{B}u_k \\ y_k = \mathbf{C}\mathbf{x}_k, \end{cases}$$

where $\mathbf{E} \in \mathbb{C}^{N \times N}$, $\mathbf{A} \in \mathbb{C}^{N \times N}$, $\mathbf{B} \in \mathbb{C}^{N \times 1}$, and $\mathbf{C} \in \mathbb{C}^{1 \times N}$ are linear operators. For $k \in \mathbb{N}$, the input, the output, and the state at time step t_k are $u_k \in \mathbb{C}$, $y_k \in \mathbb{C}$, and $\mathbf{x}_k \in \mathbb{C}^N$, respectively. The initial condition of the LTI system is $\mathbf{x}_0 = \mathbf{0}$. In the following, we assume the matrix \mathbf{E} has full rank and the system Σ is asymptotically stable, i.e., all eigenvalues of $\mathbf{E}^{-1}\mathbf{A}$ have absolute value less than 1. Note that it is important to choose the time discretization of the time-continuous LTI system (2.1) such that the resulting LTI system (2.2) is asymptotically stable. If an explicit scheme is used, this means that the time step size δt has to be chosen adequately small. We restrict the following discussion to time-discrete LTI systems that are derived via an equidistant discretization in time, i.e., via a uniform time step size.

2.2. Time-domain and frequency-domain representation of LTI systems. In the time domain, the output y_k at time step $k \in \mathbb{N}$ is the convolution of the impulse response of the system Σ and the inputs u_0, \dots, u_k

$$(2.3) \quad y_k = \sum_{i=0}^k h_i u_{k-i},$$

where the impulse response is

$$(2.4) \quad h_k = \begin{cases} \mathbf{C}(\mathbf{E}^{-1}\mathbf{A})^{k-1}(\mathbf{E}^{-1}\mathbf{B}), & k > 0 \\ 0, & k \leq 0 \end{cases}.$$

The output in the time domain can be transformed into the frequency domain with the Z-transform [37, p. 23]. Note that Σ is a time-discretized LTI system and therefore the Z-transform is used, instead of the Laplace-transform. The Z-transform of the time-domain output $\{y_k\}_{k=1}^{\infty}$ in (2.3) is the formal power series

$$Y(z) = \sum_{k=0}^{\infty} y_k z^{-k}.$$

Similarly, the Z-transform of the impulse response $\{h_k\}_{k=1}^{\infty}$ in (2.4) is the transfer function

$$(2.5) \quad H(z) = \sum_{k=0}^{\infty} h_k z^{-k}.$$

Let $U(z)$ denote the Z-transform of the time-domain input $\{u_k\}_{k=1}^{\infty}$. Then, $Y(z)$ is the multiplication of the transfer function $H(z)$ and $U(z)$, i.e.,

$$Y(z) = H(z)U(z).$$

2.3. Data-driven nonintrusive construction of reduced models from frequency-response data. The Loewner approach [5, 7, 29, 33] is a data-driven model reduction technique that derives a reduced model $\tilde{\Sigma}$ of order $n \ll N, n \in \mathbb{N}$, from frequency-response data, i.e., from values of the transfer function H of the full model Σ . The Loewner approach is therefore a nonintrusive model reduction technique. If transfer function values are available, the Loewner reduced model is derived directly from the transfer function values and does not require access to the operators of the full model.

Let $\{z_1, \dots, z_m\} \subset \mathbb{C}$ be a set of $m = 2n$ interpolation points with an arbitrary partition

$$(2.6) \quad \{z_1, \dots, z_m\} = \{\mu_1, \dots, \mu_n\} \cup \{\gamma_1, \dots, \gamma_n\}$$

into two sets of equal size. Let further $H(z_1), \dots, H(z_m)$ be the values of the transfer function—the frequency-response data—at the m interpolation points z_1, \dots, z_m . The Loewner approach constructs the Loewner matrix

$$\mathbb{L} = \begin{bmatrix} \frac{H(\mu_1) - H(\gamma_1)}{\mu_1 - \gamma_1} & \cdots & \frac{H(\mu_1) - H(\gamma_n)}{\mu_1 - \gamma_n} \\ \vdots & \ddots & \vdots \\ \frac{H(\mu_n) - H(\gamma_1)}{\mu_n - \gamma_1} & \cdots & \frac{H(\mu_n) - H(\gamma_n)}{\mu_n - \gamma_n} \end{bmatrix} \in \mathbb{C}^{n \times n}$$

and the shifted Loewner matrix

$$\mathbb{L}_s = \begin{bmatrix} \frac{\mu_1 H(\mu_1) - \gamma_1 H(\gamma_1)}{\mu_1 - \gamma_1} & \cdots & \frac{\mu_1 H(\mu_1) - \gamma_n H(\gamma_n)}{\mu_1 - \gamma_n} \\ \vdots & \ddots & \vdots \\ \frac{\mu_n H(\mu_n) - \gamma_1 H(\gamma_1)}{\mu_n - \gamma_1} & \cdots & \frac{\mu_n H(\mu_n) - \gamma_n H(\gamma_n)}{\mu_n - \gamma_n} \end{bmatrix} \in \mathbb{C}^{n \times n},$$

from the frequency-response data and the interpolation points. The Loewner reduced model is

$$(2.7) \quad \tilde{\Sigma} : \begin{cases} \tilde{\mathbf{E}} \tilde{\mathbf{x}}_{k+1} = \tilde{\mathbf{A}} \tilde{\mathbf{x}}_k + \tilde{\mathbf{B}} u_k \\ \tilde{\mathbf{y}}_k = \tilde{\mathbf{C}} \tilde{\mathbf{x}}_k, \end{cases}$$

with the operators

$$\tilde{\mathbf{E}} = -\mathbb{L}, \quad \tilde{\mathbf{A}} = -\mathbb{L}_s, \quad \tilde{\mathbf{B}} = [H(\mu_1) \quad \dots \quad H(\mu_n)]^T, \\ \text{and } \tilde{\mathbf{C}} = [H(\gamma_1) \quad \dots \quad H(\gamma_n)]$$

the reduced state $\tilde{\mathbf{x}}_k \in \mathbb{C}^n$ and the reduced output $\tilde{\mathbf{y}}_k \in \mathbb{C}$ at time step $k \in \mathbb{N}$. It is shown in [5, 29, 33] that the transfer function \tilde{H} of the Loewner reduced model interpolates the transfer function H of the full model at the interpolation points z_1, \dots, z_m . This construction assumes that the Loewner pencil $z\mathbb{L} - \mathbb{L}_s$ is invertible at every sampling point $\{z_1, \dots, z_m\}$. If this is not the case, i.e., in the case of abundant data, a post-processing step can be applied to resolve this issue by projecting the reduced operators further using a truncated singular value decomposition (SVD), see, e.g. [33] and [26, p. 150]. In [18], a post-processing step for stabilizing Loewner reduced models is presented. Moreover, if the underlying model has a singular \mathbf{E} term, i.e., it is a system of differential algebraic equations, as shown in [4], this structure can be also recovered assuming enough data is collected. Additional regularization can become necessary if the Loewner matrices are ill-conditioned [13].

The error of the reduced transfer function \tilde{H} in the \mathcal{H}_∞ norm,

$$\|H - \tilde{H}\|_{\mathcal{H}_\infty} = \sup_{|z|=1} |H(z) - \tilde{H}(z)|,$$

can be directly related to the error of the reduced output $\tilde{\mathbf{y}} = [\tilde{y}_0, \tilde{y}_1, \tilde{y}_2, \dots]^T$ in the ℓ_2 -norm

$$\|\mathbf{y} - \tilde{\mathbf{y}}\|_{\ell_2} \leq \|H - \tilde{H}\|_{\mathcal{H}_\infty} \|\mathbf{u}\|_{\ell_2},$$

where $\mathbf{y} = [y_0, y_1, y_2, \dots]^T$ and $\mathbf{u} = [u_0, u_1, u_2, \dots]^T$. Similarly, the error in the \mathcal{H}_2 norm,

$$\|H - \tilde{H}\|_{\mathcal{H}_2} = \sqrt{\frac{1}{2\pi} \int_0^{2\pi} |H(e^{j\theta}) - \tilde{H}(e^{j\theta})|^2 d\theta},$$

where $j = \sqrt{-1}$, yields

$$\|\mathbf{y} - \tilde{\mathbf{y}}\|_{\ell_\infty} \leq \|H - \tilde{H}\|_{\mathcal{H}_2} \|\mathbf{u}\|_{\ell_2}.$$

See, e.g., [10], for a discussion on the connection between frequency-domain error measures and time-domain error measures.

2.4. Problem formulation. The classical Loewner framework provides a non-intrusive way to construct a reduced model from frequency-response data (transfer function values). In contrast, our goal is to derive a Loewner reduced model from time-domain simulation data, i.e., from an output trajectory $\mathbf{y} = [y_0, \dots, y_{K-1}]^T$ that can be obtained via time-stepping the full model for a given input trajectory $\mathbf{u} = [u_0, \dots, u_{K-1}]^T$ for $K \in \mathbb{N}$ time steps. Thus, we only have available time-domain simulation data; the full-model operators and frequency-response data are unavailable in our setting. Furthermore, unlike the Loewner framework (or the interpolation framework in general) where the full model needs to be re-evaluated in the frequency domain for every interpolation point, our aim is to derive the reduced model from a *single* input/output trajectory, i.e., from data obtained from a single time-domain simulation of the full model.

3. Inferring Loewner reduced models from time-domain data. This section develops a nonintrusive data-driven technique to construct reduced models $\hat{\Sigma}$ from readily available simulation data. In particular, we require an input trajectory $\mathbf{u} \in \mathbb{C}^K$ and an output trajectory $\mathbf{y} \in \mathbb{C}^K$. Our approach first infers frequency-response data from the input and output trajectory and then uses the Loewner framework to derive an approximate Loewner reduced model from the inferred frequency-response data. Section 3.1 and Section 3.2 discuss the relationship between the time-domain data and frequency-response data. Section 3.3 introduces a regression problem to infer frequency-response data from a time-domain input/output trajectory. Section 3.4 introduces time-domain Loewner reduced models that are constructed from the inferred frequency-response data. Section 3.5 and Section 3.6 summarize the computational procedure of the time-domain Loewner approach in Algorithm 1 and provide practical considerations. Section 3.7 discusses extensions to our time-domain Loewner approach.

3.1. Relationship between time-domain and frequency-response data.

Define the points

$$(3.1) \quad q_i = e^{\frac{2\pi j}{K}i},$$

for $i = 0, \dots, K-1$. Note that $q_i \in \mathbb{D}$, for $i = 0, \dots, K-1$, where \mathbb{D} denotes the unit circle, i.e., $\mathbb{D} = \{z \in \mathbb{C} : |z| = 1\}$. It is clear from (3.1) that q_i depends on the number of time steps $K-1$. Consider the input trajectory $\mathbf{u} = [u_0, \dots, u_{K-1}]^T \in \mathbb{C}^K$ and the corresponding (discrete) Fourier coefficients vector $\mathbf{U} = [U_0, \dots, U_{K-1}]^T \in \mathbb{C}^K$ such that

$$(3.2) \quad u_k = \sum_{i=0}^{K-1} U_i q_i^k,$$

for $k = 0, \dots, K-1$. Let $r \in \mathbb{N}$ be the number of non-zero Fourier coefficients and let $\mathcal{I}_r = \{i_1, \dots, i_r\} \subseteq \{0, \dots, K-1\}$ be the set of the indices of the non-zero Fourier coefficients. This means we have $|U_i| > 0$ for $i \in \mathcal{I}_r$ and $|U_i| = 0$ for $i \in \{0, \dots, K-1\} \setminus \mathcal{I}_r$. Using the representation (3.2) in the convolution of the impulse response with the input (2.3) leads to

$$(3.3) \quad y_k = \sum_{l=0}^k h_l u_{k-l} = \sum_{l=0}^k h_l \sum_{i \in \mathcal{I}_r} U_i q_i^{k-l} = \sum_{i \in \mathcal{I}_r} U_i q_i^k \sum_{l=0}^k h_l q_i^{-l}.$$

We define the sum

$$(3.4) \quad H_k(z) = \sum_{l=0}^k h_l z^{-l}$$

for $k \in \mathbb{N}$, and rewrite (3.3) as

$$(3.5) \quad y_k = \sum_{i \in \mathcal{I}_r} U_i H_k(q_i) q_i^k.$$

For $\hat{z} \in \mathbb{D}$, the sequence of the partial sums $\{H_k(\hat{z})\}_{k=1}^{\infty}$ converges to the transfer function value $H(\hat{z})$ as $k \rightarrow \infty$, see Section 3.2 and, e.g., [2]. Thus, the relationship (3.5) provides a direct connection between the time-domain output y_k at time step k and the approximate frequency-response data $H_k(q_i)$ for $i \in \mathcal{I}_r$.

3.2. Asymptotic properties. We now analyze the convergence behavior of the sequence of the partial sums $\{H_k(\hat{z})\}_{k=1}^{\infty}$ to $H(\hat{z})$ for $\hat{z} \in \mathbb{D}$. Define $\delta H_k(\hat{z})$ such that

$$H(\hat{z}) = H_k(\hat{z}) + \delta H_k(\hat{z}),$$

for $k \in \mathbb{N}$. Proposition 3.2 shows that, as expected, the rate of the convergence of $\{\delta H_k(\hat{z})\}_{k=1}^{\infty}$ to 0 as $k \rightarrow \infty$ depends on the spectral radius of $\mathbf{E}^{-1}\mathbf{A}$. We first show Proposition 3.1 and then present Proposition 3.2. We note that Proposition 3.1 lists some basic observations about Σ , which can be found in some form or another in the literature, see, e.g., [2, Theorem 5.18]. Here we include a sketch of the proof for completeness and its connection to the later parts of the paper.

PROPOSITION 3.1. *Let $\lambda_1, \dots, \lambda_N \in \mathbb{C}$ be the poles of Σ , i.e., the eigenvalues of $\mathbf{E}^{-1}\mathbf{A}$, and let ρ denote the spectral radius, i.e.,*

$$(3.6) \quad \rho = \max_{i=1, \dots, N} |\lambda_i|.$$

Assume $\mathbf{E}^{-1}\mathbf{A}$ is diagonalizable. Then the absolute value of the impulse response h_k for $k \in \mathbb{N}$ is bounded as

$$(3.7) \quad |h_k| \leq c_1 \rho^{k-1},$$

where $c_1 \in \mathbb{C}$ is a constant independent of k . Moreover, if Σ is asymptotically stable, i.e., if $\rho < 1$, then the series

$$(3.8) \quad \sum_{k=0}^{\infty} |h_k|$$

converges.

Proof. Because $\mathbf{E}^{-1}\mathbf{A}$ is diagonalizable, we have the eigenvalue decomposition $\mathbf{E}^{-1}\mathbf{A} = \mathbf{Q}\mathbf{D}\mathbf{Q}^{-1}$, where $\mathbf{Q} \in \mathbb{C}^{N \times N}$ is the matrix of the eigenvectors of $\mathbf{E}^{-1}\mathbf{A}$ and $\mathbf{D} \in \mathbb{C}^{N \times N}$ is the diagonal matrix with the corresponding eigenvalues $\lambda_1, \dots, \lambda_N \in \mathbb{C}$. Then, plugging this into (2.4), we obtain

$$h_k = \boldsymbol{\alpha} \mathbf{D}^{k-1} \boldsymbol{\beta},$$

for $k \in \mathbb{N}$ where $\boldsymbol{\alpha} = [\alpha_1, \dots, \alpha_N] = \mathbf{C}\mathbf{Q}$ and $\boldsymbol{\beta} = [\beta_1, \dots, \beta_N]^T = \mathbf{Q}^{-1}(\mathbf{E}^{-1}\mathbf{B})$. Then, using (3.6), we obtain

$$|h_k| = |\boldsymbol{\alpha} \mathbf{D}^{k-1} \boldsymbol{\beta}| = \left| \sum_{i=1}^N \alpha_i \beta_i \lambda_i^{k-1} \right| \leq \|\boldsymbol{\alpha}\|_2 \|\boldsymbol{\beta}\|_2 \rho^{k-1},$$

with the constant

$$c_1 = \|\boldsymbol{\alpha}\|_2 \|\boldsymbol{\beta}\|_2.$$

The convergence of (3.8) follows automatically when $\rho < 1$. \square

Note that the bound in (3.7) also holds for $\rho \geq 1$. Note further that only $\rho < 1$ is necessary for the series (3.8) to converge; it is not necessary that $\mathbf{E}^{-1}\mathbf{A}$ is diagonalizable [2, Theorem 5.18].

PROPOSITION 3.2. *Let $\mathbf{E}^{-1}\mathbf{A}$ be diagonalizable and let $\hat{z} \in \mathbb{D}$ be a point on the unit circle. Then,*

$$(3.9) \quad |\delta H_k(\hat{z})| = |H(\hat{z}) - H_k(\hat{z})| \leq c_2 \rho^k,$$

where $c_2 \in \mathbb{C}$ is a constant that is independent of k and ρ is defined as in (3.6).

Proof. Using the definition of $H_k(z)$ in (3.4), we obtain

$$|H(\hat{z}) - H_k(\hat{z})| = \left| \sum_{l=k+1}^{\infty} h_l \hat{z}^{-l} \right|.$$

Since $\hat{z} \in \mathbb{D}$, we have

$$(3.10) \quad \left| \sum_{l=k+1}^{\infty} h_l \hat{z}^{-l} \right| \leq \sum_{l=k+1}^{\infty} |h_l|.$$

Then, insert (3.7) in (3.10) to obtain

$$\sum_{l=k+1}^{\infty} |h_l| \leq \sum_{l=k+1}^{\infty} c_1 \rho^{l-1} = \sum_{l=0}^{\infty} c_1 \rho^{l+k} = c_1 \rho^k \sum_{l=0}^{\infty} \rho^l = \frac{c_1}{1-\rho} \rho^k,$$

which is the desired result. \square

3.3. Inferring frequency-response data from time-domain data. We now exploit the relationship (3.5) to infer frequency-response data from a time-domain input/output trajectory of the full model. Let $0 < \epsilon \in \mathbb{R}$ be a tolerance parameter and select $k_{\min} \in \mathbb{N}$ such that $|\delta H_{k_{\min}}(q_i)| < \epsilon$ for $i \in \mathcal{I}_r$, see Section 3.6 for guidance on the selection of k_{\min} . We consider the least-squares problem

$$(3.11) \quad \hat{\mathbf{H}} = \arg \min_{\hat{H}'_1, \dots, \hat{H}'_r \in \mathbb{C}} \sum_{k=k_{\min}}^{K-1} \left(y_k - \sum_{l=1}^r U_{i_l} \hat{H}'_l q_{i_l}^k \right)^2,$$

with the solution $\hat{\mathbf{H}} = [\hat{H}'_1, \dots, \hat{H}'_r]^T \in \mathbb{C}^r$. Note that $\mathcal{I}_r = \{i_1, \dots, i_r\}$. Note further that we chose k_{\min} such that (3.11) is overdetermined and has a unique solution.

Let $\mathbf{F} \in \mathbb{C}^{(K-k_{\min}) \times r}$ be a matrix with

$$(3.12) \quad \mathbf{F} = \begin{bmatrix} U_{i_1} q_{i_1}^{k_{\min}} & \dots & U_{i_m} q_{i_r}^{k_{\min}} \\ \vdots & \ddots & \vdots \\ U_{i_1} q_{i_1}^{K-1} & \dots & U_{i_m} q_{i_r}^{K-1} \end{bmatrix} \in \mathbb{C}^{(K-k_{\min}) \times r},$$

and let $\bar{\mathbf{y}} \in \mathbb{C}^{K-k_{\min}}$ be the vector with $\bar{\mathbf{y}} = [y_{k_{\min}}, \dots, y_{K-1}]^T$. Then, (3.11) can be rewritten as the linear least-squares problem

$$(3.13) \quad \arg \min_{\hat{\mathbf{H}} \in \mathbb{C}^r} \left\| \mathbf{F} \hat{\mathbf{H}} - \bar{\mathbf{y}} \right\|_2^2,$$

which can be efficiently solved, especially if r , the number of non-zero Fourier coefficients of the input, is small. If the number of non-zero Fourier coefficients is large, the least-squares problem can become computationally expensive to solve, see the discussion in Section 3.6.

3.4. Time-domain Loewner reduced model. We first select an even number $m \leq r$ of interpolation points from the set of points $\{q_{i_1}, \dots, q_{i_r}\}$. Without loss of generality, let q_{i_1}, \dots, q_{i_m} be the interpolation points. Following the classical Loewner framework discussed in Section 2.3, the set of interpolation points $\{q_{i_1}, \dots, q_{i_m}\}$ is partitioned into two sets $\{q_{i_1}, \dots, q_{i_n}\}$ and $\{q_{i_{n+1}}, \dots, q_{i_m}\}$. As in the classical Loewner framework, our method is applicable to any partition of the set of interpolation points into two subsets of equal size.

We assemble the approximate Loewner matrix $\hat{\mathbb{L}}$ using the inferred frequency-response data $\hat{H}'_1, \dots, \hat{H}'_r$

$$(3.14) \quad \hat{\mathbb{L}} = \begin{bmatrix} \frac{\hat{H}'_1 - \hat{H}'_{n+1}}{q_{i_1} - q_{i_{n+1}}} & \dots & \frac{\hat{H}'_1 - \hat{H}'_{2n}}{q_{i_1} - q_{i_{2n}}} \\ \vdots & \ddots & \vdots \\ \frac{\hat{H}'_{i_n} - \hat{H}'_{i_{2n}}}{q_{i_n} - q_{i_{n+1}}} & \dots & \frac{\hat{H}'_{i_n} - \hat{H}'_{i_{2n}}}{q_{i_n} - q_{i_{2n}}} \end{bmatrix} \in \mathbb{C}^{n \times n}.$$

Similarly, we derive the approximate shifted Loewner matrix $\hat{\mathbb{L}}_s$

$$(3.15) \quad \hat{\mathbb{L}}_s = \begin{bmatrix} \frac{q_{i_1} \hat{H}'_1 - q_{i_{n+1}} \hat{H}'_{n+1}}{q_{i_1} - q_{i_{n+1}}} & \dots & \frac{q_{i_1} \hat{H}'_1 - q_{i_{2n}} \hat{H}'_{2n}}{q_{i_1} - q_{i_{2n}}} \\ \vdots & \ddots & \vdots \\ \frac{q_{i_n} \hat{H}'_{i_n} - q_{i_{n+1}} \hat{H}'_{i_{2n}}}{q_{i_n} - q_{i_{n+1}}} & \dots & \frac{q_{i_n} \hat{H}'_{i_n} - q_{i_{2n}} \hat{H}'_{i_{2n}}}{q_{i_n} - q_{i_{2n}}} \end{bmatrix} \in \mathbb{C}^{n \times n}.$$

We then obtain the inferred reduced operators

$$\hat{\mathbf{E}} = -\hat{\mathbb{L}}, \quad \hat{\mathbf{A}} = -\hat{\mathbb{L}}_s$$

and

$$\hat{\mathbf{B}} = [\hat{H}_1, \dots, \hat{H}_n]^T \in \mathbb{C}^{n \times 1}, \quad \hat{\mathbf{C}} = [\hat{H}_{n+1}, \dots, \hat{H}_{2n}] \in \mathbb{C}^{1 \times n}.$$

The time-domain Loewner reduced model $\hat{\Sigma}$ of order n is

$$\hat{\Sigma} : \begin{cases} \hat{\mathbf{E}}\hat{\mathbf{x}}_{k+1} = \hat{\mathbf{A}}\hat{\mathbf{x}}_k + \hat{\mathbf{B}}u_k \\ \hat{y}_k = \hat{\mathbf{C}}\hat{\mathbf{x}}_k, \end{cases}$$

with the reduced state vector $\hat{\mathbf{x}}_k \in \mathbb{C}^n$ and the reduced output $\hat{y}_k \in \mathbb{C}$ for $k \in \mathbb{N}$. Once the time-domain Loewner reduced model $\hat{\Sigma}$ is constructed, post-processing techniques to truncate [26, p. 150] and stabilize [18] the time-domain Loewner reduced model can be applied just as in the case of the classical, frequency-domain Loewner model construction.

3.5. Computational procedure. Algorithm 1 summarizes the computational procedure of deriving a time-domain Loewner reduced model. Inputs to Algorithm 1 are the input trajectory \mathbf{u} , the output trajectory \mathbf{y} , the number $k_{\min} \in \mathbb{N}$, and the dimension $n \in \mathbb{N}$ of the time-domain Loewner reduced model. First, the input trajectory \mathbf{u} is transformed into its Fourier representation with coefficients $\mathbf{U} = [U_0, \dots, U_{K-1}]^T \in \mathbb{C}^K$. The indices of the non-zero Fourier coefficients are $i_1, \dots, i_r \in \{1, \dots, K-1\}$. The matrix $\mathbf{F} \in \mathbb{C}^{(K-k_{\min}) \times m}$ and the vector $\bar{\mathbf{y}} \in \mathbb{C}^{K-k_{\min}}$ are assembled as described in Section 3.3. The matrix \mathbf{F} and the vector $\bar{\mathbf{y}}$ define the inference problem (3.13). The solution of the inference problem (3.13) are the inferred frequency-response data $\hat{H}_1, \dots, \hat{H}_r \in \mathbb{C}$ for the points q_{i_1}, \dots, q_{i_r} .

The algorithm selects the first $2n$ points $q_{i_1}, \dots, q_{i_{2n}} \in \{q_{i_1}, \dots, q_{i_r}\}$ as interpolation points. Note that our methodology is applicable to any other set of interpolation points that is a subset of $\{q_{i_1}, \dots, q_{i_r}\}$. The inferred Loewner $\hat{\mathbb{L}} \in \mathbb{C}^{n \times n}$ and the inferred shifted Loewner matrix $\hat{\mathbb{L}}_s \in \mathbb{C}^{n \times n}$ are assembled from the inferred frequency-response data $\hat{H}_{i_1}, \dots, \hat{H}_{i_{2n}}$ at the interpolation points $q_{i_1}, \dots, q_{i_{2n}}$. The time-domain Loewner reduced model $\hat{\Sigma}$ is then derived from $\hat{\mathbb{L}}$ and $\hat{\mathbb{L}}_s$ as described in Section 3.4.

The computationally expensive steps in Algorithm 1 are computing the Fourier coefficients of the input trajectory \mathbf{u} and solving inference problem (3.13). The costs of computing the Fourier coefficients are bounded in $\mathcal{O}(K \log(K))$ if the fast Fourier transform is used. The matrix \mathbf{F} is of size $(K - k_{\min}) \times r$ and therefore the costs of solving the inference problem (3.13) are bounded in $\mathcal{O}(Kr^3)$ [17, Section 5.3.3]. Typically, the runtime of computing the Fourier coefficients and the runtime of the inference are negligible compared to the runtime of time stepping the full model Σ to obtain the output trajectory \mathbf{y} for the input trajectory \mathbf{u} .

3.6. Practical considerations. The regression problem in (3.13) takes into account the outputs from time step k_{\min} to $K-1$. The outputs at time steps $1, \dots, k_{\min}-1$ are ignored because the sums $H_k(\hat{z})$ for $k = 1, \dots, k_{\min}-1$ are poor approximations of the transfer function values $H(\hat{z})$ in the sense of (3.9). The choice of the index k_{\min} is problem dependent, as indicated by the asymptotic analysis in Section 3.2. In particular, the eigenvalues of the matrix $\mathbf{E}^{-1}\mathbf{A}$ determine the convergence rate of the sequence of partial sums $\{H_k(\hat{z})\}_{k=1}^{\infty}$ to $H(\hat{z})$. Since typically the eigenvalues of $\mathbf{E}^{-1}\mathbf{A}$ are unavailable, and therefore cannot be used to guide the

Algorithm 1 Time-domain Loewner

-
- 1: **procedure** TLOEWNER($\mathbf{u}, \mathbf{y}, k_{\min}, n$)
 - 2: Define the points $q_0, \dots, q_{K-1} \in \mathbb{C}$ as in (3.1)
 - 3: Compute the Fourier coefficients $\mathbf{U} = [\hat{U}_0, \dots, \hat{U}_{K-1}]^T \in \mathbb{C}^K$ of \mathbf{u}
 - 4: Let $i_1, \dots, i_r \in \{1, \dots, K-1\}$ be the indices of the non-zero Fourier coefficients
 - 5: Assemble matrix $\mathbf{F} \in \mathbb{C}^{(K-k_{\min}) \times r}$ as in (3.12)
 - 6: Assemble vector $\hat{\mathbf{y}} = [y_{k_{\min}}, \dots, y_{K-1}]^T \in \mathbb{C}^{K-k_{\min}}$
 - 7: Solve (3.13) to infer frequency-response data $\hat{H}_1, \dots, \hat{H}_r$
 - 8: Select without loss of generality the $2n$ interpolation points $q_{i_1}, \dots, q_{i_{2n}}$
 - 9: Select the corresponding inferred data $\hat{H}_1, \dots, \hat{H}_{2n}$
 - 10: Assemble matrix $\hat{\mathbb{L}}$ using $\hat{H}_1, \dots, \hat{H}_{2n}$ as in (3.14)
 - 11: Assemble matrix $\hat{\mathbb{L}}_s$ using $\hat{H}_1, \dots, \hat{H}_{2n}$ as in (3.15)
 - 12: Construct reduced operators $\hat{\mathbf{E}} = -\hat{\mathbb{L}}, \hat{\mathbf{A}} = -\hat{\mathbb{L}}_s$
 - 13: Construct $\hat{\mathbf{B}} = [\hat{H}_1, \dots, \hat{H}_n]^T \in \mathbb{C}^{n \times 1}$ and $\hat{\mathbf{C}} = [\hat{H}_{n+1}, \dots, \hat{H}_{2n}] \in \mathbb{C}^{1 \times n}$
 - 14: Assemble time-domain Loewner reduced model $\hat{\Sigma}$ of dimension n
 - 15: **return** $\hat{\Sigma}$
 - 16: **end procedure**
-

selection of k_{\min} , we simulate the full model for many time steps $K - 1$, to ensure that the outputs enter a steady state, and then set $k_{\min} = \lfloor 1/4K \rfloor$ to use the outputs of the final 3/4 of the time steps in the inference problem (3.13). Note that setting k_{\min} too large, i.e., ignoring many outputs in the inference problem (3.13), can lead to a system matrix \mathbf{F} with a large condition number or even to an underdetermined inference problem (3.13), see the numerical results in Section 4.4.

The set of interpolation points of the time-domain Loewner reduced model $\hat{\Sigma}$ is a subset of the set of points $\{q_0, \dots, q_{K-1}\}$ defined in (3.1). This shows that increasing the number of time steps $K - 1$, increases the number of potential interpolations. The range of frequencies corresponding to the points q_0, \dots, q_{K-1} is

$$\left[\frac{2\pi}{K}, \frac{2\pi(K-1)}{K} \right] \subset \mathbb{R}.$$

Therefore, performing more time steps $K - 1$ increases the range of the frequencies of the points q_0, \dots, q_{K-1} .

The dimension of the matrix \mathbf{F} in (3.13) grows with the number of non-zero Fourier coefficients of the input. This shows that the Fourier coefficients of the input have to be sparse to make the least-squares problem (3.13) computationally tractable. Typically, one first selects interpolation points q_{i_1}, \dots, q_{i_m} of the points q_0, \dots, q_{K-1} , and then constructs a sparse input that has non-zero Fourier coefficients only for the frequencies corresponding to the interpolation points q_{i_1}, \dots, q_{i_m} . The input u_k at time step k is then a sum of m cosine and sine signals corresponding to the frequencies of q_{i_1}, \dots, q_{i_m} , i.e.,

$$u_k = \frac{1}{K} \sum_{l=1}^m (1+j) \left(\cos\left(\frac{2\pi i_l k}{K}\right) + j \sin\left(\frac{2\pi i_l k}{K}\right) \right), \quad k = 0, \dots, K-1,$$

such that the Fourier coefficients are non-zero only for frequencies $2\pi i_l k/K, l = 1, \dots, m$. Note that selecting interpolation points q_{i_1}, \dots, q_{i_m} in interpolatory model reduction is a topic of ongoing research, see, e.g., [3, 9, 10, 20].

3.7. Extensions. We presented our time-domain Loewner approach for single-input/single-output models with zero initial conditions. Here, we present a brief discussion on extensions to multi-input/multi-output systems and to non-zero initial conditions.

Consider a system with $n_{in} \in \mathbb{N}$ inputs and $n_{out} \in \mathbb{N}$ outputs. Then, $H(z_i)$ is an $n_{out} \times n_{in}$ matrix-valued rational function. In this case, in contrast to matrix interpolation, the Loewner framework (indeed, interpolatory model reduction in general) enforces tangential interpolation along a left-tangential direction $\mathbf{l}_j \in \mathbb{C}^{n_{in}}$ and a right-tangential direction $\mathbf{d}_i \in \mathbb{C}^{n_{out}}$. Then, the entries of the Loewner matrix depend on the scalars $\mathbf{l}_j^T H(z_i) \mathbf{d}_i$ for $i, j = 1, 2, \dots, r$, see, e.g., [3], for details. If, instead, matrix interpolation is preferred, then the matrix-valued quantities $H(z_i)$ will determine the Loewner matrices. This choice—matrix interpolation versus tangential interpolation—will determine what the unknowns are and whether to infer the matrix $H(z_i)$ or the scalars $\mathbf{l}_j^T H(z_i) \mathbf{d}_i$. Since the scalars $\mathbf{l}_j^T H(z_i) \mathbf{d}_i$ will be needed for all the combinations of left- and right-tangential directions, it might prove beneficial to infer $H(z_i)$ or $H(z_i) \mathbf{d}_i$ at once and recycle it to fill the entries of the Loewner model.

Consider now the situation where the full model is simulated with a non-zero initial condition. Our framework requires isolating contributions to the output due to the input only. This can be achieved by employing the superposition principle after simulating the system with zero forcing, but with the same initial condition. This approach has been recently applied in [8] for projection-based model reduction of systems with non-zero initial conditions. However, if the goal is not just to identify a reduced model, but also to use it for a wide-range of initial conditions, this requires *projecting* the new initial condition of the full-model to the reduced space. This is a topic of ongoing research even in intrusive projection-based model reduction; see, e.g., [6, 8, 24]. However, since we are only focusing on a data-driven framework here, we do not have access to internal dynamics to construct a projection subspace. To the best of our knowledge, the question of data-driven modeling with non-zero initial conditions is unanswered even in the classical Loewner framework. However, we believe that the framework of [8] might provide a feasible solution by assuming that the initial conditions of interest, although unknown, lie in a low-dimensional space spanned by a known basis.

4. Numerical results. This section demonstrates the time-domain Loewner framework on numerical examples. Section 4.1 provides numerical evidence for the bounds derived in the asymptotic analysis in Section 3. Section 4.2 and Section 4.3 derive time-domain Loewner reduced models of two benchmark models and Section 4.4 derives a time-domain Loewner reduced model of a finite element model of a cantilever beam [38].

4.1. An illustrative synthetic example. We take $N = 10$, $\mathbf{E} \in \mathbb{R}^{N \times N}$ to be the $N \times N$ identity matrix, and set $\mathbf{B} = \mathbf{C}^T$ with $\mathbf{C} = [1/N, 2/N, \dots, N/N] \in \mathbb{R}^{1 \times N}$. We construct an $N \times N$ matrix with entries drawn from a uniform distribution in $[0, 1]$. Then, we transform this matrix into the matrix \mathbf{A} such that the spectral radius of \mathbf{A} is $\rho < 1$, i.e., all the eigenvalues of \mathbf{A} lie in the unit disc. These matrices $\mathbf{E}, \mathbf{B}, \mathbf{C}$, and the matrix \mathbf{A} define a full model Σ_ρ of order $N = 10$ induced by the choice of the spectral radius ρ . We now discuss the properties of our time-domain Loewner framework on full models Σ_ρ for varying $\rho < 1$.

We first numerically investigate Proposition 3.2 and study the accuracy of the truncated sum $H_k(\hat{z})$ in approximating $H(\hat{z})$ for varying ρ values. Towards this goal

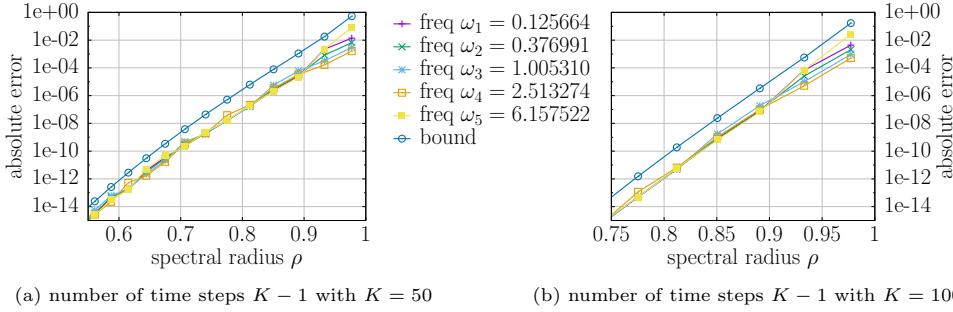


Figure 1: Illustrative example: The absolute error (4.1) of the approximations $\{H_{K-1}(q_{i_1}), \dots, H_{K-1}(q_{i_r})\}$ of the frequency-response data $\{H(q_{i_1}), \dots, H(q_{i_r})\}$ increases with the spectral radius for a fixed number of time steps. The reported results confirm numerically the bound of the absolute error derived in Proposition 3.2.

consider the $r = 5$ points on the unit circle \mathbb{D}

$$q_{i_1} = e^{j\omega_1}, q_{i_2} = e^{j\omega_2}, q_{i_3} = e^{j\omega_3}, q_{i_4} = e^{j\omega_4}, q_{i_5} = e^{j\omega_5},$$

corresponding to the frequencies in rad/s

$$\omega_1 = \frac{2\pi}{K}, \omega_2 = \frac{6\pi}{K}, \omega_3 = \frac{16\pi}{K}, \omega_4 = \frac{40\pi}{K}, \omega_5 = \frac{98\pi}{K}.$$

Figure 1 plots the absolute error

$$(4.1) \quad \text{err}_{\text{abs}}(H_{K-1}(q_i)) = |H(q_i) - H_{K-1}(q_i)|, \quad i \in \{i_1, \dots, i_r\}.$$

As expected from Proposition 3.2, for a fixed number of time steps $K - 1$, the absolute error increases with ρ . As $\rho \rightarrow 1$, the decay of the impulse response coefficients is slow, thus the truncation error of $H_{K-1}(\hat{z})$ is larger. However, as shown in Figure 1b, when K is increased to $K = 100$, the accuracy is increased. We note that if ρ is close to 1, the time-domain simulation will naturally take longer to converge. Figure 1 additionally confirms numerically the bound of the error (4.1) derived in Proposition 3.2. The plots in Figure 1 show curves for ρ for ranges where the absolute error is still within machine precision.

Next we check how the inferred frequency-response data approximate the frequency-response data of the full model. Let $\mathbf{u} = [u_0, \dots, u_{K-1}]^T \in \mathbb{C}^K$ be the input trajectory with Fourier coefficients $U_1 = 1, U_3 = 3, U_8 = 8, U_{20} = 20, U_{49} = 49$ and all other Fourier coefficients zero. Let further $\mathbf{y} = [y_0, \dots, y_{K-1}]^T \in \mathbb{C}$ be the corresponding outputs obtained via time stepping the model Σ_ρ . We approximate the full-model frequency-response data $H(q_{i_1}), \dots, H(q_{i_r})$ with the inferred frequency-response data $\hat{H}_1, \dots, \hat{H}_r$ using Algorithm 1 with $k_{\min} = \lfloor 1/4K \rfloor$. Figure 2a shows the relative error

$$(4.2) \quad \text{err}_{\text{rel}}(\hat{H}_l) = \frac{|H(q_{i_l}) - \hat{H}_l|}{|H(q_{i_l})|},$$

for $l \in \{1, \dots, r\}$ and for varying ρ . Figure 2b shows the relative errors (4.2) for $K = 100$ and $l = 1, \dots, r$. The theory presented in Section 3.2 suggests that the relative error of the inferred frequency-response data depends on the spectral radius

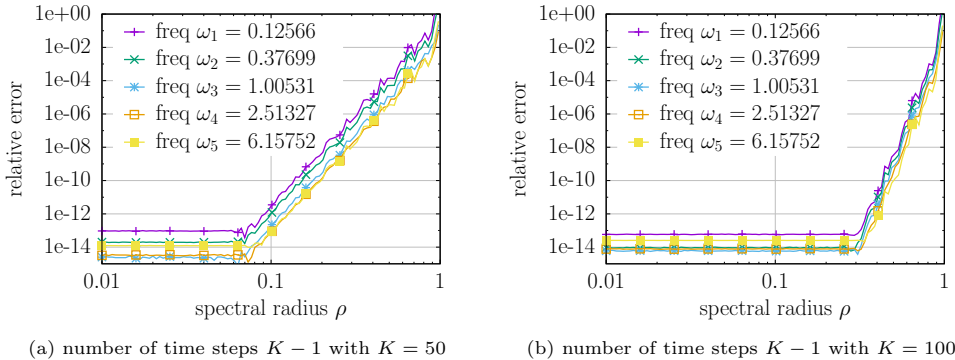


Figure 2: Illustrative example: The plots show that the relative error of the inferred frequency-response data $\{\hat{H}_1, \dots, \hat{H}_r\}$ is large if the spectral radius is large relative to the number of time steps $K - 1$. In (a), where $K = 50$, the error starts to increase significantly near $\rho = 7 \times 10^{-2}$, and in (b), where $K = 100$, the error starts to increase near $\rho = 3 \times 10^{-1}$.

ρ , which is confirmed by the results reported in Figure 2a and Figure 2b. For a fixed number of time steps, a large spectral radius ρ leads to a large error. Increasing the number of time steps helps to reduce the error, as can be seen by comparing Figure 2a with Figure 2b. Thus, with an appropriately chosen K value, Algorithm 1 accurately infers frequency-response data for a wide range of ρ values.

Figure 3 demonstrates that, besides increasing the number of time steps K , increasing the parameter k_{\min} can compensate a larger ρ value. Recall that our time-domain Loewner approach ignores all outputs at time steps $1, \dots, k_{\min} - 1$ and uses the outputs at time steps $k_{\min}, \dots, K - 1$ in the regression problem to infer frequency-response data. In Figure 3a, the frequency-response data are inferred with a relative error of about 10^{-12} for spectral radii in the range $\rho \in [10^{-2}, 7 \times 10^{-2}]$ for $k_{\min} = \lfloor 1/4K \rfloor$ and in the range $[10^{-2}, 4 \times 10^{-1}]$ for $k_{\min} = \lfloor 3/4K \rfloor$. Thus, increasing k_{\min} significantly increases the range of spectral radii for which transfer function values are accurately inferred. A similar behavior is reported in Figure 3b for $K = 100$. Note that setting k_{\min} too large can lead to a system matrix \mathbf{F} of (3.13) with a large condition number and introduce numerical errors into the inferred data, see the detailed discussion in Section 4.4.

4.2. Eady example. We consider the dynamics of baroclinic instabilities as described by Eady’s model [16]. Baroclinic instabilities are the dominant mechanism that shape cyclones in the atmosphere and are typically found in the mid-latitude regions of the Earth. We consider here a time-continuous LTI system of a baroclinic instability, i.e., a storm track, which is a common model reduction benchmark example¹. We discretize the LTI system with the fourth-order Dormand-Prince method [14] and time step size $\delta t = 10^{-1}$ to obtain a full model Σ of the form (2.2). We set $K = 10^3$ so that the points q_0, \dots, q_{K-1} have frequencies in the range

$$[2\pi \times 10^{-3}, 2\pi \times (1 - 10^{-3})].$$

We are interested in the frequency range $[2\pi \times 10^{-3}, 3]$. Note that we chose the time step size large to demonstrate the time-domain Loewner approach on an ex-

¹<http://slicot.org/20-site/126-benchmark-examples-for-model-reduction>

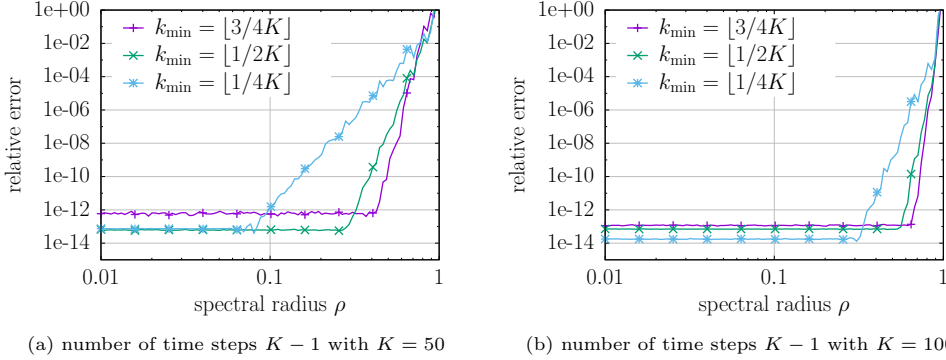


Figure 3: Illustrative example: The inference (3.13) uses time-domain outputs starting at time step k_{\min} . Setting k_{\min} large relative to the number of time steps $K - 1$, avoids the outputs at early time steps where the approximations $H_k(\hat{z})$ have a large error, see Proposition 3.2.

ample where we have available outputs at only few time steps. We set $n = 8$, $m = 64$, and $k_{\min} = \lfloor 1/4K \rfloor$, see Section 3.6. The interpolation points $q_{i_1}, \dots, q_{i_{m/2}} \in \{q_0, \dots, q_{K-1}\}$ are selected as logarithmically equidistant frequencies in the range $[2\pi \times 10^{-3}, 3]$, and the points $q_{i_{m/2+1}}, \dots, q_{i_m}$ are their complex conjugates so that both Loewner models have real state-space realizations. The input trajectory $\mathbf{u} = [u_0, \dots, u_{K-1}]^T \in \mathbb{C}^K$ has the components

$$u_k = \frac{1}{K} \sum_{l=1}^m (1 + j) \left(\cos\left(\frac{2\pi i_l k}{K}\right) + j \sin\left(\frac{2\pi i_l k}{K}\right) \right), \quad k = 0, \dots, K - 1,$$

so that we obtain the Fourier coefficients

$$(4.3) \quad U_i = \begin{cases} 1 + j, & \text{if } i \in \{i_1, \dots, i_m\}, \\ 0, & \text{else,} \end{cases}$$

for $i = 0, \dots, K - 1$. We feed the input \mathbf{u} to the full model Σ , run a single time-domain simulation, and derive the time-domain Loewner reduced model $\hat{\Sigma}$ with Algorithm 1. Subsequently, we perform the truncation step discussed in [26, p. 150] to reduce the dimension of the reduced model to $n = 8$. For comparison, we additionally construct the classical Loewner reduced model $\tilde{\Sigma}$.

The magnitude and phase of the full model, the classical Loewner reduced model, and the time-domain Loewner reduced model are shown in Figure 4. The transfer functions are evaluated at 100 test points on the unit circle with frequencies logarithmically distributed in the range $[2\pi \times 10^{-3}, 3]$. As the figure shows, the time-domain Loewner reduced model captures the behavior of the classical Loewner reduced model accurately. Figure 5 shows the output trajectory of a time-domain simulation of the time-domain Loewner, the classical Loewner, and the full model for a non-zero input and a zero initial condition. The output trajectory of the time-domain Loewner reduced model achieves a similar approximation quality with respect to the full model as the output trajectory of the classical Loewner reduced model. The \mathcal{H}_2 and \mathcal{H}_∞ errors [10] of the two reduced models are shown in Table 1. The crucial observation

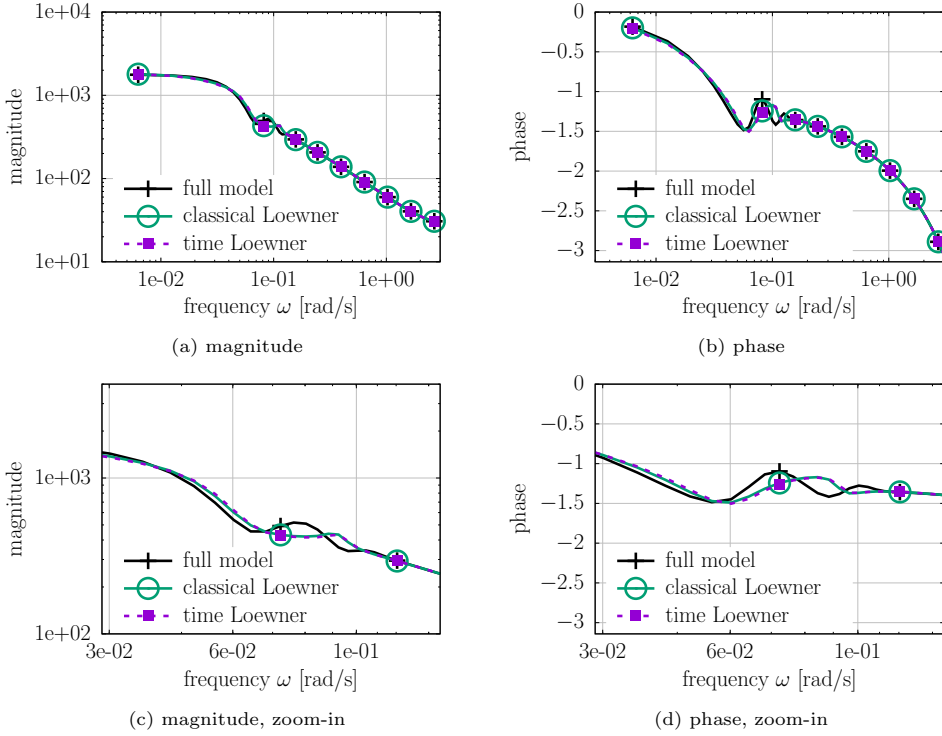


Figure 4: Eady example: The plots compare the magnitude and the phase of the transfer function of the time-domain and the classical Loewner reduced model to the full model.

here is that with a single time-domain simulation and without any frequency-response data, Algorithm 1 mimics the accuracy of the classical Loewner model, which requires evaluating the transfer function at every interpolation point.

Figure 6a compares the eigenvalues of the matrix $\hat{\mathbf{E}}^{-1}\hat{\mathbf{A}}$ of the time-domain Loewner reduced model to the corresponding eigenvalues of the classical Loewner reduced model. Figure 6b plots the magnitude of the eigenvalues. The time-domain Loewner reduced model, and the classical Loewner reduced model, are both asymptotically stable. Additionally, the poles of the time-domain Loewner model approximate the poles of the classical Loewner model well.

4.3. Penzl example. We consider Penzl’s time-continuous LTI system introduced in [41, Example 3], which is investigated in the context of the Loewner approach in [26, p. 151] and in the context of SVD-Krylov-based model reduction methods in [2, p. 408]. Define the following matrices

$$\bar{\mathbf{A}}_1 = \begin{bmatrix} -1 & 100 \\ -100 & -1 \end{bmatrix}, \quad \bar{\mathbf{A}}_2 = \begin{bmatrix} -1 & 200 \\ -200 & -1 \end{bmatrix}, \quad \bar{\mathbf{A}}_3 = \begin{bmatrix} -1 & 400 \\ -400 & -1 \end{bmatrix},$$

and the diagonal matrix $\bar{\mathbf{A}}_4 \in \mathbb{R}^{1000 \times 1000}$ with $-1, -2, \dots, -1000$ on the diagonal. The matrix $\bar{\mathbf{A}} \in \mathbb{R}^{1006 \times 1006}$ is a block-diagonal matrix with $\bar{\mathbf{A}}_1, \bar{\mathbf{A}}_2, \bar{\mathbf{A}}_3, \bar{\mathbf{A}}_4$ on the diagonal. The matrices $\mathbf{B} \in \mathbb{R}^{1006}$ and $\mathbf{C} \in \mathbb{R}^{1 \times 1006}$ are defined as

$$\mathbf{B}^T = \mathbf{C} = [10 \ 10 \ 10 \ 10 \ 10 \ 10 \ 1 \ \dots \ 1].$$

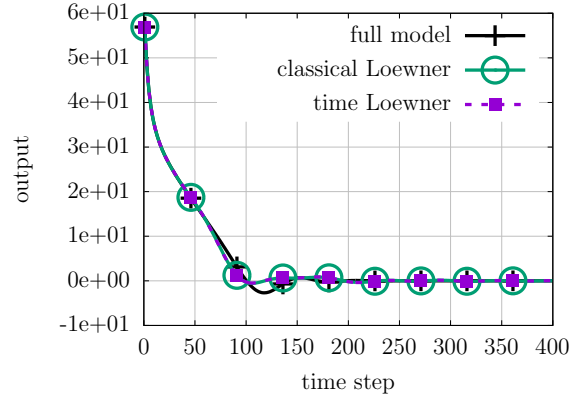


Figure 5: Eady example: In this example, the time-domain output trajectory of the time-domain Loewner model has a similar approximation accuracy as the output trajectory of the classical Loewner model with respect to the full model.

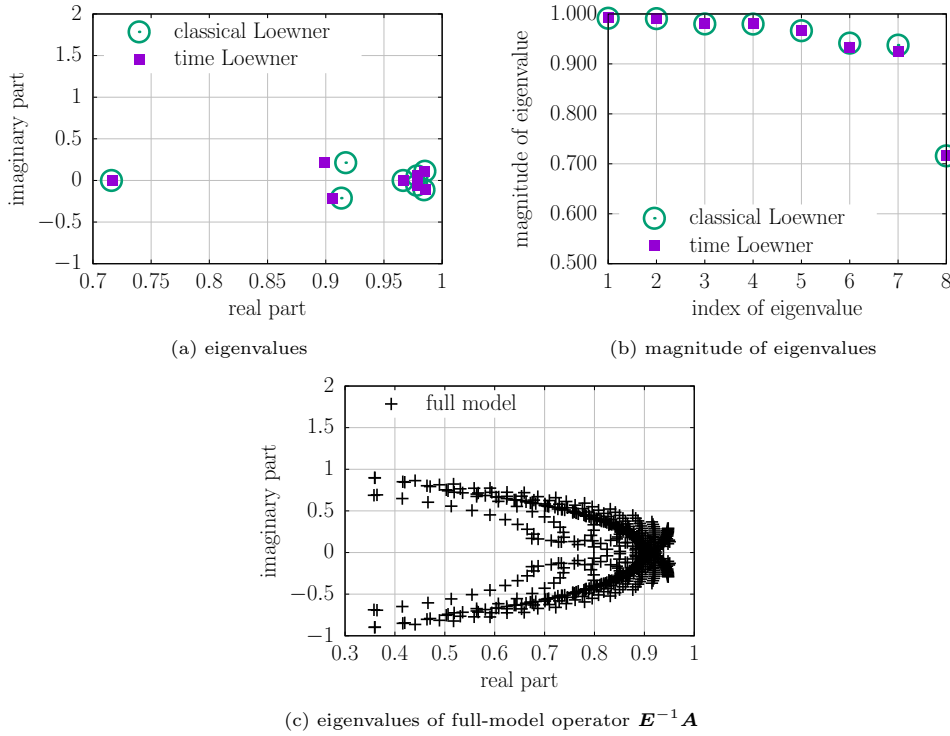


Figure 6: Eady example: The eigenvalues of $\hat{E}^{-1}\hat{A}$ of the time-domain Loewner reduced model are similar to the corresponding eigenvalues of the classical Loewner reduced model. The magnitude of the eigenvalues is less than 1 and therefore the time-domain Loewner reduced model is asymptotically stable.

Table 1: The \mathcal{H}_2 and the \mathcal{H}_∞ error of the transfer function of the classical \tilde{H} and the time-domain Loewner \hat{H} with respect to the full model transfer function H .

	$\frac{\ H-\tilde{H}\ _{\mathcal{H}_2}}{\ H\ _{\mathcal{H}_2}}$	$\frac{\ H-\hat{H}\ _{\mathcal{H}_2}}{\ H\ _{\mathcal{H}_2}}$	$\frac{\ \tilde{H}-\hat{H}\ _{\mathcal{H}_2}}{\ H\ _{\mathcal{H}_2}}$
eady	7.41×10^{-2}	7.54×10^{-2}	1.46×10^{-2}
penzl	2.47×10^{-1}	2.47×10^{-1}	1.19×10^{-4}
beam	4.56×10^{-3}	6.17×10^{-3}	6.13×10^{-3}

	$\frac{\ H-\tilde{H}\ _{\mathcal{H}_\infty}}{\ H\ _{\mathcal{H}_\infty}}$	$\frac{\ H-\hat{H}\ _{\mathcal{H}_\infty}}{\ H\ _{\mathcal{H}_\infty}}$	$\frac{\ \tilde{H}-\hat{H}\ _{\mathcal{H}_\infty}}{\ H\ _{\mathcal{H}_\infty}}$
eady	5.56×10^{-2}	6.03×10^{-2}	1.53×10^{-2}
penzl	1.35×10^{-1}	1.35×10^{-1}	1.91×10^{-4}
beam	5.88×10^{-4}	8.03×10^{-4}	6.93×10^{-4}

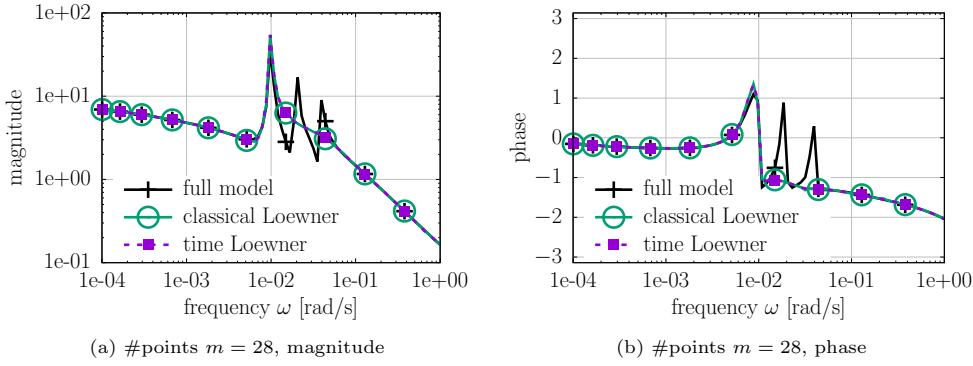


Figure 7: Penzl example: The plots show the magnitude and the phase of the transfer functions evaluated at 100 test points. The time-domain Loewner reduced model yields similar results as the classical Loewner reduced model.

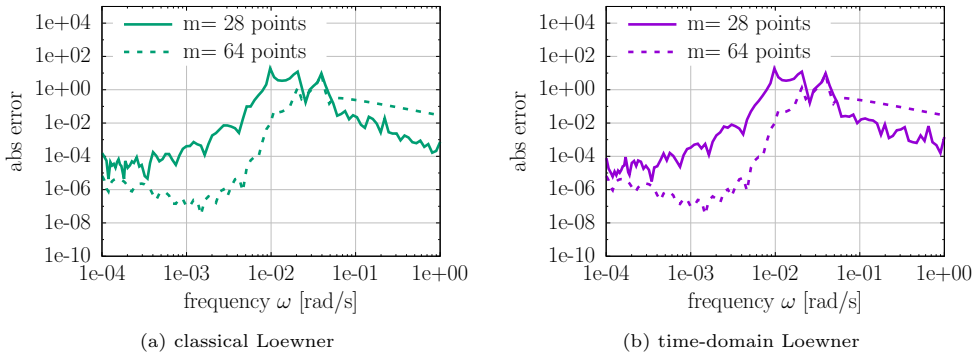


Figure 8: Penzl example: The absolute error (4.1) of the transfer function of the time-domain Loewner reduced model over 100 test points shows a similar behavior as the absolute error corresponding to the classical Loewner reduced model.

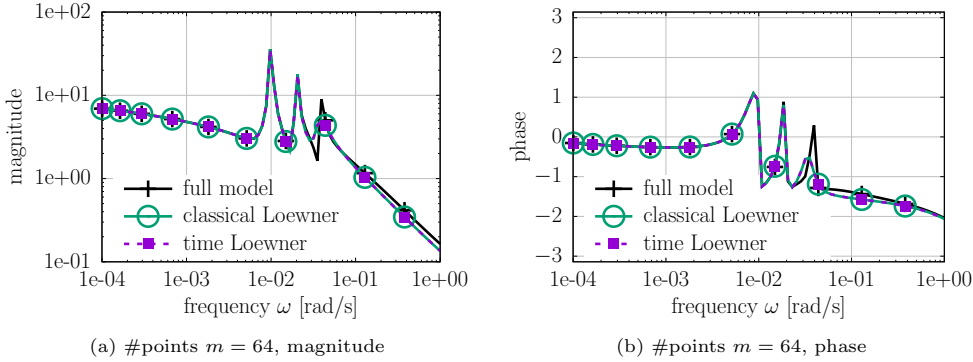


Figure 9: Penzl example: Increasing the number m of interpolation points from $m = 2n = 28$ to $m = 64$ increases the approximation quality of the time-domain Loewner reduced model near the poles, cf. Figure 7.

We discretize the time-continuous LTI system given by

$$\begin{aligned} \dot{\mathbf{x}}(t) &= \bar{\mathbf{A}}\mathbf{x}(t) + \mathbf{B}u(t) \\ y(t) &= \mathbf{C}\mathbf{x}(t) \end{aligned}$$

in time with the implicit Euler method and time step size $\delta t = 10^{-4}$ to obtain a full model Σ of the form (2.2). We set $K = 10^6$ so that the frequency range of the points q_0, \dots, q_{K-1} defined in (3.1) is

$$(4.4) \quad [2\pi \times 10^{-6}, 2\pi \times (1 - 10^{-6})] .$$

Following [26, p. 151], we restrict the discussion to the frequency range $[10^{-4}, 1]$, which contains the significant part of the frequency domain response of Σ . We set $n = 14$, $m = 2n = 28$, and $k_{\min} = \lceil 1/4K \rceil$, see Section 3.6. The first $m/2$ interpolation points $q_{i_1}, \dots, q_{i_{m/2}} \in \{q_0, \dots, q_{K-1}\}$ are selected as logarithmically equidistant frequencies in the range $[10^{-4}, 1]$, and the other $m/2$ interpolation points such that the set is closed under complex conjugation. The input trajectory $\mathbf{u} = [u_0, \dots, u_{K-1}]^T \in \mathbb{C}^K$ is derived as in Section 4.2. We then time step the full model Σ for this input \mathbf{u} , a single time-domain simulation, to obtain the outputs $\mathbf{y} = [y_0, \dots, y_{K-1}]^T \in \mathbb{C}^K$ and derive the time-domain Loewner reduced model $\hat{\Sigma}$ with Algorithm 1. For comparison, we additionally construct the classical Loewner reduced model $\tilde{\Sigma}$.

The magnitude and the phase of the transfer function of the full model, the classical Loewner reduced model, and the time-domain Loewner reduced model are shown in Figure 7. As before, the transfer function is evaluated at 100 test points on the unit circle with frequencies logarithmically distributed in the range $[10^{-4}, 1]$. The time-domain Loewner reduced model provides a similar approximation accuracy in magnitude as the classical Loewner reduced model. Two peaks in the magnitude and the phase of the transfer function are missed by the classical and the time-domain Loewner reduced model. Our results below will show that increasing the number of interpolation points leads to classical and time-domain Loewner reduced models that capture the peaks in the transfer function more accurately. The absolute error of the transfer function of the time-domain Loewner reduced model is plotted in Figure 8 and illustrates once more that both models have almost the same accuracy.

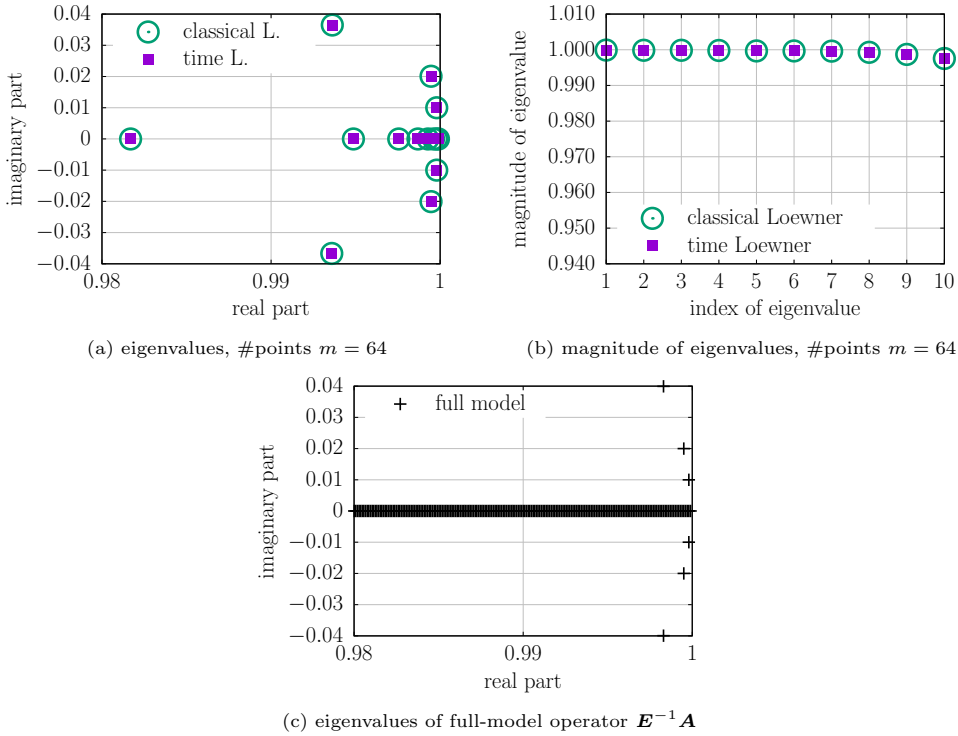


Figure 10: Penzl example: The eigenvalues of $\hat{E}^{-1}\hat{A}$ of the time-domain Loewner reduced model are similar to the corresponding eigenvalues of the classical Loewner reduced model. The magnitude of the eigenvalues is less than 1 and therefore the time-domain Loewner reduced model is asymptotically stable.

Figure 9 shows that increasing the number of interpolation points from $m = 28$ to $m = 64$, and subsequently performing the truncation step discussed in [26, p. 150] to reduce the dimension of the reduced model to $n = 14$, increases the accuracy of the time-domain Loewner reduced model even further. The two Loewner models approximate the first two peaks in the transfer function of the full model well and miss the third peak. Note, however, that the time-domain Loewner reduced model matches the classical Loewner reduced model well. The absolute errors plotted in Figure 8 confirm that the time-domain and the classical Loewner reduced model have a similar error in the frequency range $[10^{-4}, 1]$ rad/s. For $m = 64$, the errors in the \mathcal{H}_2 and \mathcal{H}_∞ norm are reported in Table 1, illustrating that the \mathcal{H}_2 and \mathcal{H}_∞ performance of the time-domain Loewner captures that of the classical Loewner at least to the third significant digit. The eigenvalues of $\hat{E}^{-1}\hat{A}$ of the time-domain Loewner reduced model are shown in Figure 10 and confirm that the model is asymptotically stable and matches the poles of the classical Loewner model as before.

4.4. Cantilever beam. We now consider a finite element model of a cantilever Timoshenko beam in a three-dimensional spatial domain [38]. The geometry of the beam is shown in Figure 11a. The length of the beam is 1 and the height and thickness of the beam is 0.01. Young's modulus is set to 210×10^9 N/m² and the density is 7850 kg/m³, which are typical parameters for iron. Poisson's ratio is 3/10. The input is the

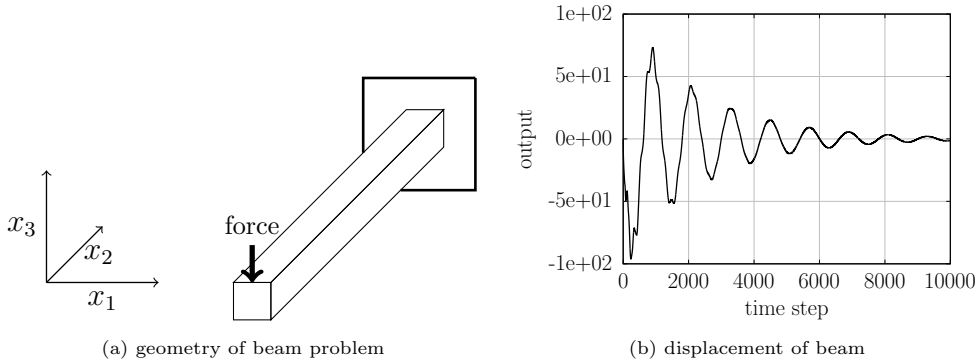


Figure 11: Beam example: The geometry of the beam problem is shown in (a). The plot in (b) shows the displacement of the tip of the beam in direction x_3 in response to a non-zero input at time 0.

force on the tip of the beam in direction x_3 . The output is the deflection of the beam at the tip in direction x_3 . We discretize the corresponding time-continuous LTI system in time with the implicit Euler method with time step size $\delta t = 10^{-4}$ and set $K = 10^6$ to time step the corresponding full model Σ for $K - 1$ time steps. The dimension of the full model is $N = 240$. The impulse/response of the LTI system is shown in Figure 11b. The frequency range of the sampling points (3.1) is equal to the frequency range (4.4) of the Penzl example. The input trajectory $\mathbf{u} = [u_0, \dots, u_{K-1}]^T \in \mathbb{C}^K$ has the Fourier coefficients (4.3) for $m = 132$ logarithmically distributed frequencies in the range (4.4) such that they are closed under complex conjugation. We time step the full model Σ with the corresponding input trajectory to obtain the output trajectory $\mathbf{y} = [y_0, \dots, y_{K-1}]^T \in \mathbb{C}^K$.

Consider first the choice of the parameter k_{\min} . The results in Section 4.1 and Figure 3 suggest setting k_{\min} large relative to the number of time steps $K - 1$ so that only the outputs at the later time steps are used in the inference problem (3.13); however, setting k_{\min} too large can result in a system matrix \mathbf{F} of the inference problem (3.13) with a large condition number. Figure 12 shows the condition number of the matrix \mathbf{F} for values $k_{\min} \in \{2.5 \times 10^5, 5 \times 10^5, 7.5 \times 10^5, 9 \times 10^5, 9.9 \times 10^5, 9.99 \times 10^5\}$. The reported results in Figure 12 illustrate for this example that the condition number of \mathbf{F} is large if k_{\min} is large, i.e., if many output samples are ignored in the inference problem.

As in the Penzl example and as discussed in Section 3.6, we set $k_{\min} = \lfloor 1/4K \rfloor = 2.5 \times 10^5$ and derive a time-domain Loewner reduced model of dimension $n = 8$ using Algorithm 1. We additionally construct the classical Loewner reduced model with the same interpolation points for comparison. Figures 13a and 13b show the magnitude and the phase of the full model, the classical Loewner reduced model, and the time-domain Loewner reduced model evaluated at 100 test points corresponding to logarithmically distributed frequencies in the range (4.4). The time-domain Loewner reduced model captures the full model very accurately, especially for low frequencies. For higher frequencies, i.e., in the frequency range $[10^{-1}, 1]$ rad/s, the time-domain Loewner reduced model provides a poor approximation of the full model. However, the classical Loewner reduced model is inaccurate in this high frequency range as well. Thus, further increasing the number of interpolation points and the dimension of the

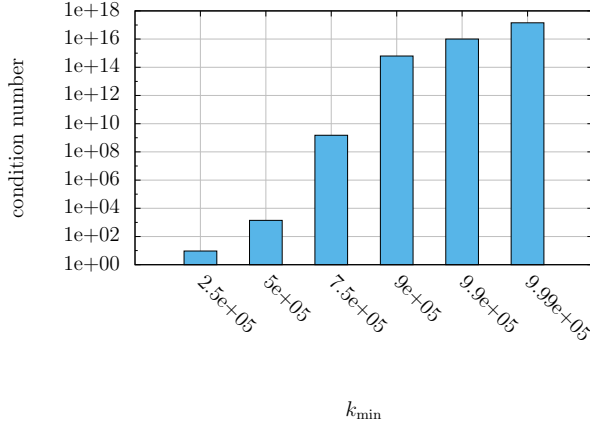


Figure 12: Beam example: The condition number of the system matrix \mathbf{F} of the inference problem (3.13) significantly depends on the parameter k_{\min} . If k_{\min} is set large relative to the number of time steps $K - 1$, i.e., if many outputs are ignored in the inference problem (3.13), then the condition number of \mathbf{F} can become large and induce numerical errors in the inferred frequency-response data.

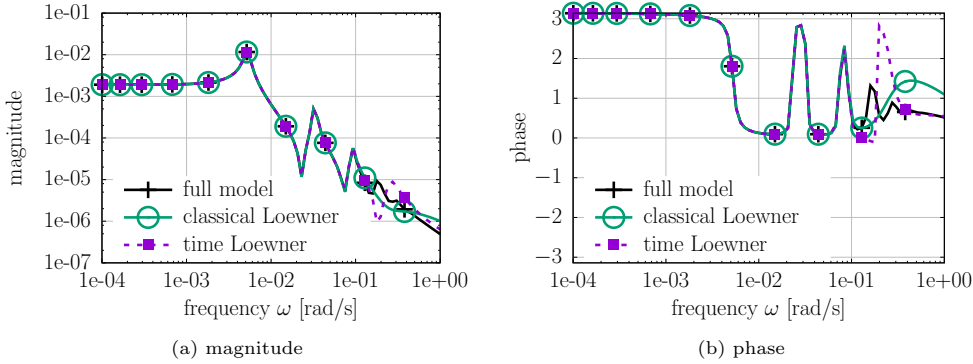


Figure 13: Beam example: The time-domain Loewner reduced model provides a similar approximation quality as the classical Loewner reduced model.

reduced models might be necessary to approximate well the transfer function in the high frequency range.

The absolute error of the transfer function of the time-domain Loewner reduced model is similar to the error of the classical Loewner reduced model, see Figure 14a, once again justifying the time-domain Loewner model achieves the accuracy of the classical Loewner model. We provide a time-domain simulation of the time-domain Loewner model and classical Loewner model. The outputs of the classical and the time-domain Loewner reduced model in response to non-zero inputs and zero initial conditions are plotted in Figure 14b, showing that the time-domain response of both models are almost the same. The response of the full model is plotted in Figure 11b and visualized in Figure 15. Figures 16a and 16b show that the time-domain and the

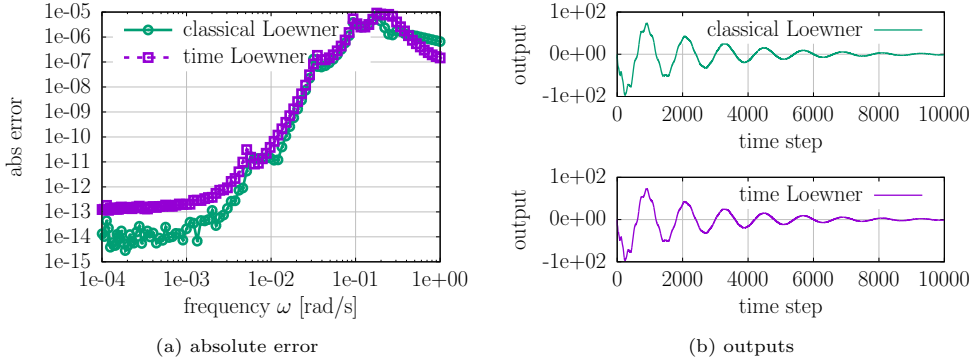


Figure 14: Beam example: The plot in (a) shows that the absolute error of the time-domain and the classical Loewner reduced model behaves similar in this example. The plot (b) compares the output of the time-domain and the classical Loewner reduced model.

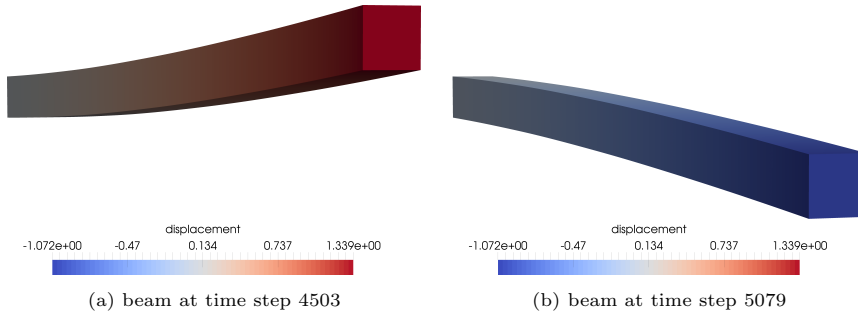


Figure 15: Beam example: The plot shows the displacement of the beam in direction x_3 . Note that the displacement, length, width, and height of the beam are scaled for the visualizations.

classical Loewner reduced models are asymptotically stable.

We now derive a time-domain Loewner reduced model from four different inputs than the input we constructed as defined in (4.3). We consider a sine signal

$$u_k^{\text{sine}} = \sin\left(\frac{f_B k}{K}\right), \quad k = 0, \dots, K-1,$$

with $f_B = 25$, and a “chirp” signal

$$u_k^{\text{chirp}} = \sin\left(1 + 2\pi\left(f_A \frac{k}{K} + \frac{(f_B - f_A)k^2}{2K^2}\right)\right) - \sin(1), \quad k = 0, \dots, K-1,$$

with $f_A = 10^{-2}$. The inputs $\mathbf{u}^{\text{sine}} = [u_0^{\text{sine}}, \dots, u_{K-1}^{\text{sine}}]^T$ and $\mathbf{u}^{\text{chirp}} = [u_0^{\text{chirp}}, \dots, u_{K-1}^{\text{chirp}}]^T$ are visualized in Figure 17a-b, respectively. Additionally, we consider the “square” input $\mathbf{u}^{\text{square}}$ that is constructed with the `square` method of MATLAB with frequency $2\pi/f_B$, and the “sawtooth” input $\mathbf{u}^{\text{sawtooth}}$ that is constructed with the `sawtooth` method of MATLAB with frequency $2\pi/f_B$, see Figure 17c-d. Consider now the Fourier coefficients $\mathbf{U}^{\text{sine}} \in \mathbb{R}^K$, $\mathbf{U}^{\text{chirp}} \in \mathbb{R}^K$, $\mathbf{U}^{\text{square}} \in \mathbb{R}^K$, and $\mathbf{U}^{\text{sawtooth}} \in \mathbb{R}^K$ of the inputs \mathbf{u}^{sine} , $\mathbf{u}^{\text{chirp}}$, $\mathbf{u}^{\text{square}}$, and $\mathbf{u}^{\text{sawtooth}}$, respectively. We set all Fourier coefficients

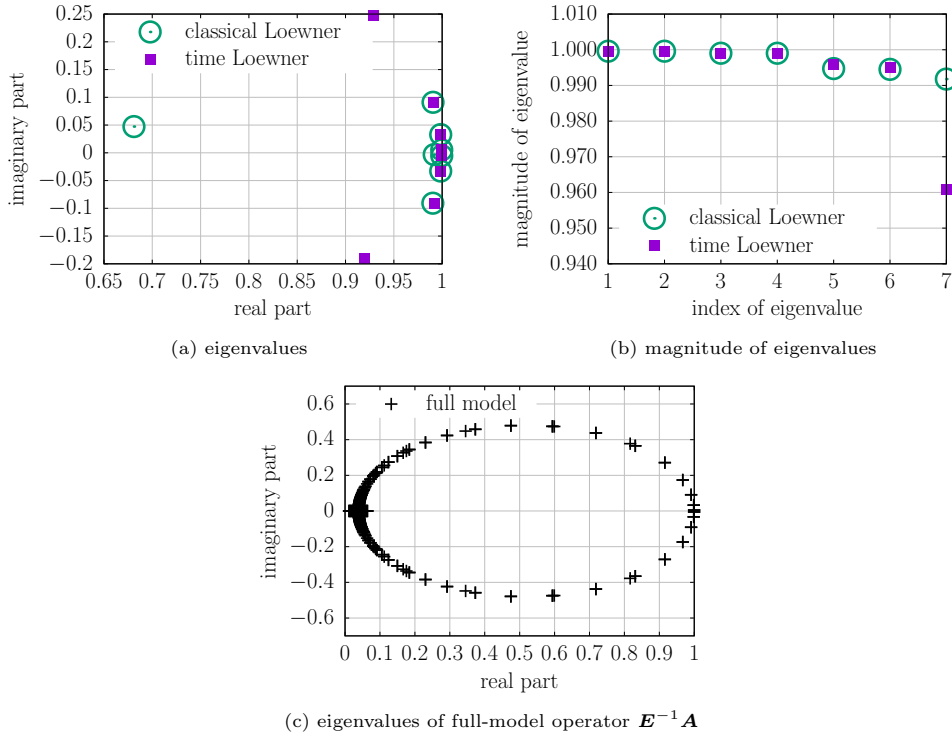


Figure 16: Beam example: The time-domain Loewner reduced model of dimension $n = 8$ with $m = 132$ interpolation points is asymptotically stable.

to zero except those that correspond to the $m = 132$ logarithmically distributed frequencies in the range (4.4), cf. the construction of the input above. This sparsification leads to the inputs $\hat{\mathbf{u}}^{\text{sine}}$, $\hat{\mathbf{u}}^{\text{chirp}}$, $\hat{\mathbf{u}}^{\text{square}}$, and $\hat{\mathbf{u}}^{\text{sawtooth}}$ in the time domain, for which we run Algorithm 1. The magnitudes of the transfer functions of the corresponding time-domain Loewner reduced models are shown in Figure 18. All inputs lead to a similar behavior as the synthetic input used above. This illustrates Algorithm 1 is not restricted to a specific input and provides flexibility and robustness for various input selections.

5. Conclusions. We presented a time-domain Loewner framework that constructs a reduced model of an LTI system (e.g., stemming from the discretization of a time-dependent linear PDE) directly from a single time-domain input/output trajectory. Our framework is applicable to black-box full models that are marched forward in time to compute the outputs for given inputs but for which the operators of the full model and frequency-response data are unavailable. Our approach infers frequency-response data from the input/output trajectory of the full model and then uses the classical Loewner framework to construct a reduced model. The numerical results demonstrate that the time-domain Loewner reduced models provide a similar accuracy as the classical Loewner reduced models in our examples with benchmark and finite element models. Extending the new time-domain Loewner framework to multi-input/multi-output LTI systems and moving from Lagrange interpolation that

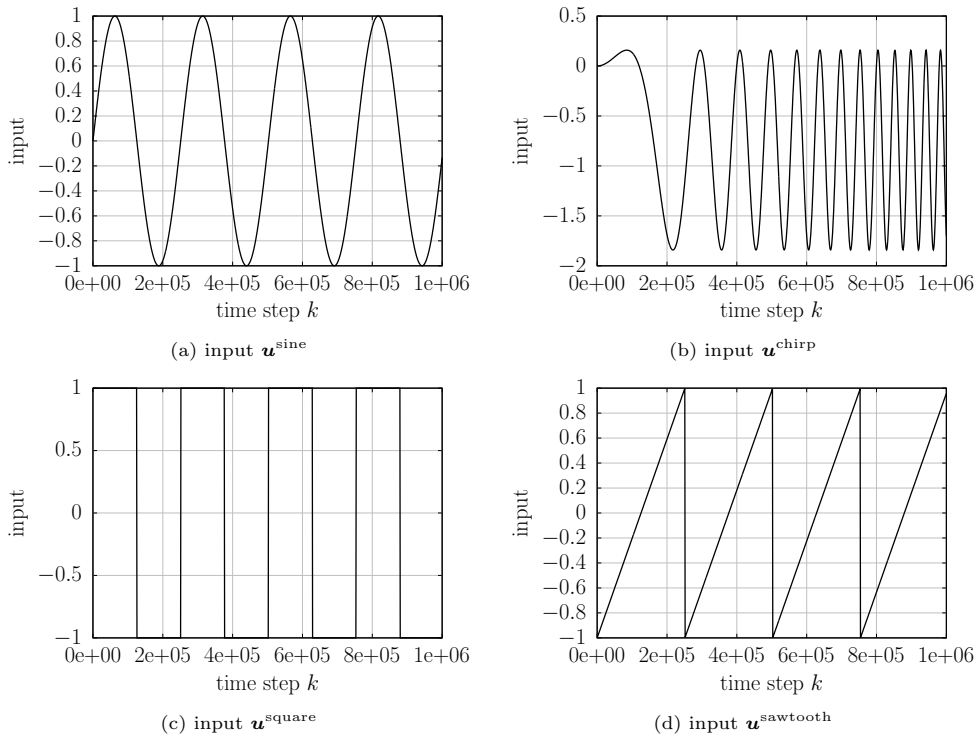


Figure 17: Beam example: The plot visualizes the sine \mathbf{u}^{sine} , the chirp $\mathbf{u}^{\text{chirp}}$, the square $\mathbf{u}^{\text{square}}$, and the sawtooth $\mathbf{u}^{\text{sawtooth}}$ inputs.

we consider here to Hermite interpolation are important directions of ongoing and future work. We developed our time-domain Loewner approach for time-discrete LTI systems (2.2) that are obtained via a time discretization with equidistant time step size. Future work includes an extension to adaptive time step sizes, which will require a formulation of our time-domain Loewner approach for LTI systems with time-varying operators.

Acknowledgments. The work of S. Gugercin was supported in part by NSF through Grant DMS-1522616 and by the Alexander von Humboldt Foundation. The work of the first and third author was supported in part by NSF through Award 1507488, CBET Program Manager D. Papavassiliou. Several examples were computed on the computer clusters of the Munich Centre of Advanced Computing.

REFERENCES

- [1] K. Abderrahim, H. Mathlouthi, and F. Msahli. New approaches to finite impulse response systems identification using higher-order statistics. *IET Signal Processing*, 4(5):488–501, 2010.
- [2] A. Antoulas. *Approximation of Large-Scale Dynamical Systems*. SIAM, 2005.
- [3] A. Antoulas, C. Beattie, and S. Gugercin. Interpolatory model reduction of large-scale dynamical systems. In J. Mohammadpour and K. Grigoriadis, editors, *Efficient Modeling and Control of Large-Scale Systems*. Springer-Verlag, 2010.

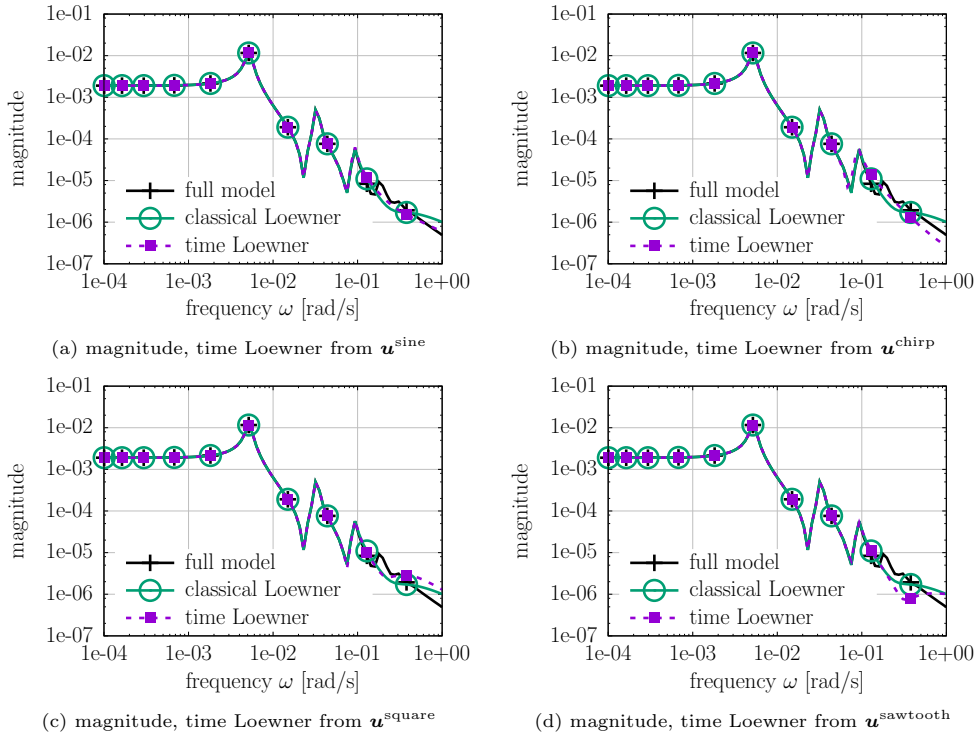


Figure 18: Beam example: The time-domain Loewner reduced models constructed from the sine \mathbf{u}^{sine} , the chirp $\mathbf{u}^{\text{chirp}}$, the square $\mathbf{u}^{\text{square}}$, and the sawtooth $\mathbf{u}^{\text{sawtooth}}$ input lead to transfer functions that approximate the transfer function of the full model with a similar accuracy as the transfer function of the time-domain Loewner reduced model obtained from the synthetic input.

- [4] A. C. Antoulas. The Loewner framework and transfer functions of singular/rectangular systems. *Applied Mathematics Letters*, 54:36–47, 2016.
- [5] A. C. Antoulas and B. D. Q. Anderson. On the scalar rational interpolation problem. *IMA Journal of Mathematical Control & Information*, 3(2-3):61–88, 1986.
- [6] O. Bashir, K. Willcox, O. Ghattas, B. van Bloemen Waanders, and J. Hill. Hessian-based model reduction for large-scale systems with initial-condition inputs. *International Journal for Numerical Methods in Engineering*, 73(6):844–868, 2008.
- [7] C. Beattie and S. Gugercin. Realization-independent \mathcal{H}_2 -approximation. In *Proc. IEEE Conf. Decis. Control*, pages 4953–4958, Maui, HI, USA, 2012.
- [8] C. Beattie, S. Gugercin, and V. Mehrmann. Model reduction for systems with inhomogeneous initial conditions. *Systems & Control Letters*, 99:99 – 106, 2017.
- [9] P. Benner and T. Breiten. Interpolation-based \mathcal{H}_2 -model reduction of bilinear control systems. *SIAM Journal on Matrix Analysis and Applications*, 33(3):859–885, 2012.
- [10] P. Benner, S. Gugercin, and K. Willcox. A survey of projection-based model reduction methods for parametric dynamical systems. *SIAM Review*, 57(4):483–531, 2015.
- [11] G. Berkooz, P. Holmes, and J. L. Lumley. The proper orthogonal decomposition in the analysis of turbulent flows. *Annu. Rev. Fluid Mech.*, 25(1):539–575, 1993.
- [12] S. L. Brunton, J. L. Proctor, and J. N. Kutz. Discovering governing equations from data by sparse identification of nonlinear dynamical systems. *Proceedings of the National Academy of Sciences*, 113(15):3932–3937, 2016.
- [13] S. L. Campbell, P. Kunkel, and V. Mehrmann. Chapter 2: Regularization of linear and nonlinear descriptor systems. In L. T. Biegler, S. L. Campbell, and V. Mehrmann, editors, *Control and Optimization with Differential-Algebraic Constraints*, pages 17–36. SIAM, 2012.

- [14] J. Dormand and P. Prince. A family of embedded Runge-Kutta formulae. *Journal of Computational and Applied Mathematics*, 6(1):19 – 26, 1980.
- [15] M. Drohmann, B. Haasdonk, and M. Ohlberger. Reduced basis approximation for nonlinear parametrized evolution equations based on empirical operator interpolation. *SIAM Journal on Scientific Computing*, 34(2):A937–A969, 2012.
- [16] E. T. Eady. Long waves and cyclone waves. *Tellus*, 1(3):33–52, 1949.
- [17] G. H. Golub and C. F. V. Loan. *Matrix Computations*. Johns Hopkins University Press, 2013.
- [18] I. V. Gosea and A. C. Antoulas. Stability preserving post-processing methods applied in the Loewner framework. In *2016 IEEE 20th Workshop on Signal and Power Integrity (SPI)*, pages 1–4, 2016.
- [19] M. A. Grepl, Y. Maday, N. C. Nguyen, and A. T. Patera. Efficient reduced-basis treatment of nonaffine and nonlinear partial differential equations. *ESAIM: Mathematical Modelling and Numerical Analysis*, 41(03):575–605, 2007.
- [20] S. Gugercin, A. Antoulas, and C. Beattie. \mathcal{H}_2 Model Reduction for Large-Scale Linear Dynamical Systems. *SIAM Journal on Matrix Analysis and Applications*, 30(2):609–638, Jan. 2008.
- [21] B. Haasdonk and M. Ohlberger. Reduced basis method for finite volume approximations of parametrized linear evolution equations. *ESAIM: M2AN*, 42(2):277–302, 2008.
- [22] J. Heiland and V. Mehrmann. Distributed control of linearized Navier-Stokes equations via discretized input/output maps. *ZAMM - Journal of Applied Mathematics and Mechanics / Zeitschrift für Angewandte Mathematik und Mechanik*, 92(4):257–274, 2012.
- [23] J. Heiland, V. Mehrmann, and M. Schmidt. A new discretization framework for input/output maps and its application to flow control. In R. King, editor, *Active Flow Control II: Papers Contributed to the Conference "Active Flow Control II 2010", Berlin, Germany, May 26 to 28, 2010*, pages 357–372, Berlin, Heidelberg, 2010. Springer Berlin Heidelberg.
- [24] M. Heinkenschloss, T. Reis, and A. Antoulas. Balanced truncation model reduction for systems with inhomogeneous initial conditions. *Automatica*, 47(3):559 – 564, 2011.
- [25] J. Hokanson. *Numerically Stable and Statistically Efficient Algorithms for Large Scale Exponential Fitting*. PhD thesis, Rice University, 2013.
- [26] A. C. Ionita. *Lagrange rational interpolation and its applications to approximation of large-scale dynamical systems*. PhD thesis, Rice University, 2013.
- [27] A. C. Ionita and A. C. Antoulas. *Matrix pencils in time and frequency domain system identification*, pages 79–88. Control, Robotics and Sensors. Institution of Engineering and Technology, 2012.
- [28] B. Kramer and S. Gugercin. The eigensystem realization algorithm from tangentially interpolated data. *Mathematical and Computer Modelling of Dynamical Systems*, 2016. to appear.
- [29] S. Lefteriu and A. Antoulas. A new approach to modeling multiport systems from frequency-domain data. *Computer-Aided Design of Integrated Circuits and Systems, IEEE Transactions on*, 29(1):14–27, Jan 2010.
- [30] L. Ljung. *System identification*. Prentice Hall, 1987.
- [31] Y. Maday, A. Patera, J. D. Penn, and M. Yano. PBDW state estimation: Noisy observations; configuration-adaptive background spaces; physical interpretations. *ESAIM: Proc.*, 50:144–168, 2015.
- [32] J. Mann and J. N. Kutz. Dynamic mode decomposition for financial trading strategies. *Quantitative Finance*, 0(0):1–13, 0.
- [33] A. Mayo and A. Antoulas. A framework for the solution of the generalized realization problem. *Linear Algebra and its Applications*, 425(2–3):634 – 662, 2007.
- [34] J. Mendel. Tutorial on higher-order statistics (spectra) in signal processing and system theory: theoretical results and some applications. *Proc. IEEE*, 79:278–305, 1991.
- [35] B. Moore. Principal component analysis in linear systems: Controllability, observability, and model reduction. *IEEE Transactions on Automatic Control*, 26(1):17–32, Feb. 1981.
- [36] C. Mullis and R. Roberts. Synthesis of minimum roundoff noise fixed point digital filters. *IEEE Transactions on Circuits and Systems*, 23(9):551–562, Sept. 1976.
- [37] K. Ogata. *Discrete Time Control Systems*. Prentice-Hall, 1995.
- [38] H. Panzer, J. Hubele, R. Eid, and B. Lohmann. Generating a parametric finite element model of a 3D cantilever Timoshenko beam using Matlab. Technical report, Chair of Automatic Control, Technische Universität München, 2009.
- [39] E. J. Parish and K. Duraisamy. A paradigm for data-driven predictive modeling using field inversion and machine learning. *Journal of Computational Physics*, 305:758 – 774, 2016.
- [40] B. Peherstorfer and K. Willcox. Data-driven operator inference for nonintrusive projection-based model reduction. *Computer Methods in Applied Mechanics and Engineering*, pages –,

- 2016.
- [41] T. Penzl. Algorithms for model reduction of large dynamical systems. *Linear Algebra and its Applications*, 415(2–3):322 – 343, 2006.
 - [42] J. L. Proctor, S. L. Brunton, B. W. Brunton, and J. N. Kutz. Exploiting sparsity and equation-free architectures in complex systems. *The European Physical Journal Special Topics*, 223(13):2665–2684, 2014.
 - [43] J. L. Proctor, S. L. Brunton, and J. N. Kutz. Dynamic mode decomposition with control. *SIAM Journal on Applied Dynamical Systems*, 15(1):142–161, 2016.
 - [44] S. J. Qin. An overview of subspace identification. *Computers & Chemical Engineering*, 30(10–12):1502 – 1513, 2006.
 - [45] L. Rabiner, R. Crochiere, and J. Allen. FIR system modeling and identification in the presence of noise and with band-limited inputs. *IEEE Transactions on Acoustics, Speech, and Signal Processing*, 26(4):319–333, 1978.
 - [46] E. Reynders. System identification methods for (operational) modal analysis: Review and comparison. *Archives of Computational Methods in Engineering*, 19(1):51–124, 2012.
 - [47] G. Rozza, D. Huynh, and A. Patera. Reduced Basis Approximation and a Posteriori Error Estimation for Affinely Parametrized Elliptic Coercive Partial Differential Equations. *Archives of Computational Methods in Engineering*, 15(3):229–275, Sept. 2008.
 - [48] A. P. Singh, K. Duraisamy, and Z. J. Zhang. Augmentation of Turbulence Models Using Field Inversion and Machine Learning. In *55th AIAA Aerospace Sciences Meeting*, AIAA SciTech Forum. American Institute of Aeronautics and Astronautics, Jan. 2017.
 - [49] L. Sirovich. Turbulence and the dynamics of coherent structures. *Quarterly of Applied Mathematics*, pages 561–571, 1987.
 - [50] J. H. Tu, C. W. Rowley, D. M. Luchtenburg, S. L. Brunton, and J. N. Kutz. On dynamic mode decomposition: Theory and applications. *Journal of Computational Dynamics*, 1(2):391–421, 2014.
 - [51] M. Viberg. Subspace-based methods for the identification of linear time-invariant systems. *Automatica*, 31(12):1835 – 1851, 1995. Trends in System Identification.
 - [52] M. Yano, J. D. Penn, and A. T. Patera. A model-data weak formulation for simultaneous estimation of state and model bias. *Comptes Rendus Mathematique*, 351(23–24):937 – 941, 2013.